Dynamic role of monocytes and meningeal macrophages in bacterial meningoencephalitis

Vitka Gres[1,2], Florens Lohrmann[1,2], Vidmante Fuchs[3,4], Lance Fredrick Pahutan Bosch[3,4], Anne Lösslein[1,2], Jana Neuber[1,2,3], Zohreh Mansoori Moghadam[1,2,3], Tiago Martins[1,2,3], Sebastian Baasch[1,2], Julia Henschel[3,4], Mirjam Freudenhammer[1,2], Marco Prinz[4], Katrin Kierdorf [4,5],Julia Kolter[1,2,5], Daniel Erny[4]*, Philipp Henneke[1,2*#]

[1] Institute for Immunodeficiency, Center for Chronic Immunodeficiency, Medical Center and Faculty of Medicine, University of Freiburg, Freiburg, Germany

[2] Institute for Infection Control and Prevention, Medical Center and Faculty of Medicine, University of Freiburg, Freiburg, Germany

[3] Faculty of Biology, University of Freiburg, Freiburg, Germany

[4] Institute of Neuropathology, Faculty of Medicine, University of Freiburg, Freiburg, Germany

[5] Centre for Integrative Biological Signalling Studies (CIBSS), University of Freiburg, Freiburg, Germany

* Equal contribution

[#] Correspondence: philipp.henneke@uniklinik-freiburg.de

Keywords: meningoencephalitis, dura mater, CNS, monocytes, macrophages

1. Abstract

Macrophages in the dura mater are substantial contributors to the immune defense of the brain, however, their site-specific origin and function in bacterial infections of the central nervous system are incompletely understood.
In a natural model of streptococcal meningoencephalitis, where bacteria systemically spread via the bloodstream to the brain, we found streptococci to be largely restricted in the meninges. Further sporadic spread of bacteria to the underlying brain parenchyma caused a region-restricted microglia activation. Invasion of monocytes, but not granulocytes into brain and leptomeninges correlated to the disease severity. Inflammation in the dura was accompanied by activation and loss of dural macrophages, and by the rapid engraftment of highly activated monocytes. In addition, monocyte progenitors in the skull marrow underwent drastic changes and acquired a more immature phenotype likely due to infection-induced emergency myelopoiesis. Notably, while dural monocytes were derived from adjacent skull marrow in a CCR2-independent fashion, the high demand for dural monocytes in streptococcal meningoencephalitis required intact CCR2 signalling and involved the long bone marrow, indicating heterogeneity in monocyte recruitment. Furthermore, meningoencephalitis increased monocyte progeny from monocyte-dendritic cell progenitors compared to the homeostatic, granulocyte-monocyte progenitor-dominated origin. Accordingly, monocytes in the dura, recruited from distinct reservoirs depending on disease-inherent needs, are intertwined with the disease course and may thus offer opportunities for therapeutic interventions.

2. Introduction

Bacterial meningoencephalitis is a devastating disease that affects millions of people each year. Group B Streptococcus (*Streptococcus agalactae*, GBS) is a common colonizer of the gastrointestinal and urogenital tract, but also a leading cause of neonatal meningoencephalitis. It also poses a risk to patients with diabetes mellitus, pregnant women, the elderly, and immunocompromised[1]. GBS meningoencephalitis has mortality rates up to 10% while surviving patients often suffer from neurological sequelae [2,3].

The brain's integrity is protected by anatomical barriers ensuring a controlled passage of molecules from the periphery to the central nervous system (CNS). The choroid plexus, perivascular space along the vasculature and meninges host resident populations of macrophages (Macs), together called CNS-associated Macs (CAM). They have important

roles in maintaining homeostasis of the CNS, but also provide neuroprotection in many pathologies [4–7]. Anatomically, the meninges consist of three layers – dura, arachnoid and pia mater[8]. The dura comprises a complex immunological landscape, including T- and B- cells, NK cells, neutrophils, plasmacytoid dendritic cells, conventional DCs, mast cells, monocytes, and diverse subsets of the most abundant population - Macs[9]. Dural sinuses that drain venous blood represent sites of antigen sampling and presentation[10]. The dura is connected to the skull marrow via ossified channels which provide a direct migratory route for monocytes, neutrophils and B-cells[11,12]. It was recently described that cerebrospinal fluid may transport bacteria from the dura to the skull marrow when bacteria like *Streptococcus pneumoniae* were directly injected into the cisterna magna[13]. However, the dynamics of the dura–skull marrow immune axis in blood-borne bacterial infection remains unclear.

In contrast to the dura, the brain parenchyma contains only one resident immune population in a steady state – microglia (MG). In a healthy brain, it is highly unlikely for MG to encounter peripheral immune cells like neutrophils or monocytes. In contrast, neuroinflammatory conditions, e.g., multiple sclerosis[14] or ischemic stroke[15], can lead to blood-brain barrier leakiness and infiltration of leukocytes, leading to MG activation and exacerbation of the disease.

In GBS infection of the brain, neuroimmune communication appears to be crucial. On one hand, MG have been implicated to exacerbate the infection, e.g., by producing nitric oxide which ultimately leads to neuronal death[16]. On the other hand, trigeminal ganglia nociceptors located in the dura dampen the Mac immune response through CGRP-RAMP1 signalling, leading to an escalation of bacterial spread to the brain parenchyma[17]. However, a deeper understanding of immune cell dynamics in the CNS and particularly its borders during streptococcal meningoencephalitis is lacking.

Here, we studied the discrete immune responses of MG, DM, and infiltrating monocytes to streptococcal meningoencephalitis caused by haematogenous spread. We took an integrated approach to understand the intersectionality of myeloid fates in the infection with a focus on localisation and differentiation trajectories. Thus, we identified DM to take the centre stage in meningoencephalitis with specific fate and activation patterns. Infiltrating monocytes actively replenished resident DM and were imprinted by their spatial and cellular origin. This emphasizes that bacterial infection induces fundamental ontogenetical and functional changes in tissue-resident Macs, and that the recruitment pathways and differentiation dynamics of migrating monocytes intertwined with disease progression, providing opportunities for therapeutic intervention.

3. Results

3.1 Haematogenous spread of GBS causes rapid brain inflammation

Previous studies on the immune responses in bacterial meningoencephalitis in mice frequently relied on disease models involving direct pathogen inoculation into the cisterna magna[9,14,15], therefore circumventing the effect of peripheral immune activation and systemic bacterial dissemination on CNS inflammation. However, in streptococcal meningoencephalitis, colonization of mucous membranes usually precedes CNS infection, and bacterial dissemination through blood is observed in many cases. In order to analyse a more physiological model where meningoencephalitis results from haematogenous bacterial spread, we intravenously injected mice with $5x10^7$ CFU of the serotype III hypervirulent BM110 GBS strain, previously associated with neonatal meningoencephalitis[18,19]. The infection spread expeditiously, and the general fitness of the infected mice rapidly declined until 3 day post infection (dpi) when half of the mice lost more than 20% of their body weight, leading to termination of the experiments (Suppl. Fig. 1a). Hence, for further experiments, we focused on earlier time points. At 2 dpi, bacteria were present in blood, brain, dural meninges, liver, skull and femur (Fig. 1a). In agreement with previous data on sepsis[20], interleukin (IL)-6 levels in the plasma (Suppl. Fig. 1b) as well as tumour necrosis factor (TNF)-α, IL-1β and interferon (IFN)-β in the brain lysates of infected mice were substantially increased (Suppl. Fig. 1c).

Next, we spatially explored GBS spread in the brain parenchyma and meningeal barriers. We found only few scattered GBS in the parenchyma, while leptomeninges contained large bacterial clusters (Fig. 1b, c). In dural whole mounts, GBS clusters were found in the proximity of the sinuses (Fig. 1d) suggesting that immune processes in the meninges are able to halt bacterial dissemination and restrain the bacteria at the barrier. The antibacterial immune response in meningeal barriers is commonly associated with the cost of an increase in blood-brain barrier permeability[2,21] leading to the infiltration of bacterial effectors, but just as well monocytes and neutrophils in the parenchyma. Furthermore, activation of MG has previously been implicated as an early response in bacterial meningoencephalitis propagating leukocyte recruitment to the brain[22]. We found that MG, CAM (including leptomeningeal, perivascular and choroid plexus Macs) and neutrophil populations did not significantly expand in the infection, while monocyte numbers in the brain were highly increased (Fig. 1e, Suppl. Fig. 1d). In fact, monocyte influx positively correlated with the bacterial burden the brain, as severely infected mice had more than 50 -fold increased monocyte numbers compared to less affected mice (Fig. 1f). Although the neutrophil influx positively correlated to the bacterial burden as well, the difference in linear regression slopes was several orders of magnitude lower as compared to monocytes (Fig. 1f). In contrast, both monocytes and neutrophils were

significantly increased in the dura during GBS infection (Fig. 1g, Suppl. Fig. 1e). While the homeostatic dura was inhabited by a compact network of CX_3CR1^+ DM, their density was reduced in the GBS infected dura (Fig. 1g, h). Collectively, these data show that systemic streptococcal infection drastically affects the immune cell composition of the brain and the dura.

3.2. MG and DM share a type-I interferon response to GBS infection

Next, we investigated the specific responses of the dynamically changing resident myeloid compartment in GBS infection in two distinct CNS compartments – dural meninges and parenchyma. In the recently described *Mrc1*$^{CreER/CreER}$*;R26*$^{Tomato/Tomato}$ fate mapping mouse line, tamoxifen (TAM) induction enables labelling of CAM, including DM, by Tomato due to their high *Mrc1* expression, whereas MG do not express *Mrc1* and remain unlabelled (Suppl. Fig. 2b)[23]. Accordingly, we infected these mice with GBS 8 weeks after TAM induction to ensure that monocyte-derived cells emerging post infection were not labelled (Fig. 2a). We then sorted DM [CD45^{hi} CD11b^{hi} Ly6C^{neg} Ly6G^{neg} Tomato^{pos} (Fig. 2b)] and MG [CD45^{low} CD11b^{hi} Ly6C^{neg}Ly6G^{neg}Tomato^{neg} (Fig. 2c)] and performed bulk RNA sequencing (RNA-seq). Principal component analysis (PCA) showed distinct clustering of the isolated populations, corresponding to their location-specific functions (Fig. 2d). However, whereas control and infected MG clustered closely together, DM from infected or uninfected mice showed a distinct gene expression profile. In line with our previous report [23] many of the upregulated differentially expressed (DE) genes in DM and MG after GBS infection were associated with type I IFN signalling and with the defence response to bacteria, e.g., *Oasl2, Irf7, Usp18, Fcgr4, Gbp2, Ifit1, Plac8, Oas3, Isg15,* and *Ifi44,* implying the existence of a common resident Mac response to GBS that is type I IFN-driven (Fig. 2e). Of note, relative expression levels of these genes were significantly higher in DM than in MG post infection (Fig. 2e,f). Indeed, when comparing upregulated DE genes in each population, DM upregulated genes associated to defence response, such as *Serpinb1a, Parp9, Ccl6, Ccl8, Ccl12, C3* and *Chil3* (Fig. 2g). In contrast, when we looked into associated gene ontology (GO) terms in MG, we found many genes related to cell cycle, mitosis and nuclear division, indicating that the infection disrupted the fine balance between MG apoptosis and proliferation[24] (Fig. 2h), whereas GO terms associated to "immune response to pathogen" were not prominently featured. Next, we analysed whether the specific localization at the immunologically dynamic CNS border primed DM to more inflammatory phenotype already in a steady state. As expected, both cell populations showed specific signature genes which were differentially expressed for both populations, such as *Cx3cr1*, *Tmem119, P2ry12* and *Sall1* for MG, or *Cbr2, Mrc1, Pf4* and *Cd163* for DM (Suppl. Fig. 2c). In addition, many inflammatory genes were elevated in steady state DM, particularly

Il-1β and genes of major histocompatibility complex II compared to MG (Fig. 2i). Enriched GO terms of DM during steady state were connected to immune response and cytokine production (Suppl. Fig. 2d), while MG GO terms reflected homeostatic MG functions (Suppl. Fig. 2e). In summary, in comparison to immunologically "indolent" MG, DM are transcriptionally primed for fast inflammatory response to be executed in streptococcal meningoencephalitis.

3.3 MG responses to the infection are dependent on association with bacteria

MG are a major contributor to brain homeostasis, pruning synapses and phagocytosing debris[25]. Since an exaggerated inflammatory response leads to neuronal damage[16], MG activation needs to be tightly controlled. In cases homeostatic conditions are disrupted, e.g., by GBS infiltration, they are equipped with a well-identified repertoire of pattern-recognition receptors involved in GBS sensing, including TLR2, TLR7, TLR13 and NLRP3[6,25–27]. Therefore, we wondered if activation of MG during GBS infection could be seen as a function of disease severity. For that purpose, we measured expression of inflammatory genes such as *Tnf*, *Il1b* and chemokines *Cxcl1* and *Ccl2* from sorted MG from mice with different bacterial burden. Indeed, MG activation positively correlated to the GBS load in the brain (Fig. 3a). MG have unique morphological features that are often used as a readout of their homeostatic or inflammatory phenotype [26,27], furthermore subtle changes in morphology can already indicate alterations in MG network homeostasis and disturbance of brain homeostasis. To further understand these potentially subtle alterations induced in the spatial organization of the MG network of mice with moderate or high bacterial counts in the brain (Fig. 3b), we performed high resolution confocal imaging of MG in the cortical area and employed high-throughput automated cell morphometry pipeline, 3DMorph[28]. This pipeline allows unbiased 3D reconstruction of individual cells with subsequent skeletonisation and the readout of different morphological parameters, which identify alterations in MG morphology (Fig. 3c).

Interestingly, while cell volumes of MG from mice with a moderate or high burden were similarly increased (Fig. 3d), MG of severely infected mice were significantly less ramified, compared both to control and moderately infected brains (Fig. 3e). Additionally, while moderately infected MG occupied larger cell territories with longer processes compared to control MG, severely infected MG seemed to return back to the baseline by occupying less volume and retracting their processes (Fig. 3f-g). This is in line with previous reports demonstrating that in the case of injury, microglia swiftly extend their processes. Yet, if extensive damage occurs, they processes are again shortened, while low ramification is kept, leading to amoeboid morphology [27,29].

Furthermore, in infected brains MG in a close proximity to leptomeninges (which contained most GBS) appeared morphologically different from MG at more distal sites (Fig. 3h). To further explore this phenomenon, we compared the cell volumes and ramification index of MG up to 140 µm below the leptomeninges, and more distal MG (Suppl. Fig. 3a). While the cell volumes of both groups were comparable, the leptomeningeal-associated MG showed much lower ramification (Fig. 3i). Therefore, MG activation appears to be influenced by spatial association with bacteria.

3.4. Increased diversity of dural myeloid cells in infection

Previous reports showed that the neuroinflammatory conditions allow for monocyte engraftment in both the parenchyma and in the meninges[21,22,30,31]. We therefore wondered if the changes in resident DM and MG highlighted above are associated with high monocyte influx and possible infection-driven monocyte-to-Mac differentiation.

Accordingly, we first investigated the dynamics of monocyte engraftment into the resident tissue Mac population in steady state by using *Cxcr4*$^{CreER/+}$;*R26*$^{Tomato/+}$ mouse model, in which TAM induction labels hematopoietically-derived cells, including monocyte progenitors, monocytes and neutrophils for up to six months[32]. In steady state, MG are seeded early in embryonic development and do not receive substantial input from peripheral monocytes [33,34], therefore they remained unlabelled throughout the experiment (Suppl. Fig. 4a). On the other hand, Macs in the dura showed a gradual replacement by circulating monocytes, reaching up to 30% after 8 weeks and about 50% after 16 weeks (Suppl. Fig. 4a).

Next, we assessed whether the infection impacted Mac differentiation dynamics in dura and brain. Thus, we induced *Cxcr4*$^{CreER/+}$;*R26*$^{Tomato/+}$ mice with TAM for 8 weeks, followed by infection and analysis at 2 dpi (Fig. 4a). While we did not detect Tomato^{+} MG-like cells in the brain parenchyma, we found increased frequency of CD206^{+}Tomato^{+} DM after infection compared to the steady state, implying faster recruitment and/or differentiation of monocyte-derived cells during meningoencephalitis (Fig. 4b). In addition, GBS infection was associated with the expansion of a distinct population of Macs that expressed both CD206 and Ly6C (Fig. 4c, d). In *Cxcr4*$^{CreER/+}$;*R26*$^{Tomato/+}$ mice, these cells were exclusively Tomato^{+}, indicating that they directly originate from labelled HSCs and their progeny from the bone marrow. (Suppl. Fig. 4b). Of note, these subset of Macs upregulated MHC-II, while Ly6C^{+} monocytes in the dura were MHC-II negative (Fig. 4e). Therefore, this population likely represented a transient monocyte-to-Mac differentiation stage, which fuels the DM population upon infection and replaces resident DM with HSC-derived progenitors. In order to further explore the complexity of myeloid population dynamics, we applied single-cell transcriptional analysis on

CD45^{+}CD11b^{+} cells isolated by FACS sorting from control and GBS infected dura. Unbiased hierarchical clustering analysis revealed 12 distinct cell clusters out of which three represented DM populations [clusters 0-2, (Fig. 4f)]. All Mac clusters expressed the canonical DM genes, e.g., *Pf4, Fcgr1, Cx3cr1* and *Mrc1* (Fig. 4g). Cluster 1 represented the previously reported MHC-II positive DM population, which expressed higher levels of *Cd81, Ccr2* and *Cd14* compared to other Mac clusters, and was reported to be of monocyte origin[35,36] (Fig. 4g, h). Clusters 0 and 2 represented tissue-resident populations, with cluster 2 expressing more *Mertk* and *Cd163* compared to other two DM clusters (Fig. 4g). Cluster 0 exhibited upregulated expression of type I IFN regulated genes, such as *Isg15, Irf7, Ifit2, Ifitm3, Cxcl10, Ifit1* in steady state compared to the cluster 1 and 2 (Fig. 4h, i). Therefore, we defined Mac population 0 as "IFN-associated" DM. Next, we identified a cDC population expressing *Cd209a, H2-Ab1* and *Slamf7* (cluster 7), classical monocytes expressing *Ly6c* and *Ccr2* (cluster 6) and patrolling, non-classical monocytes (cluster 5) expressing *Nr4a1* and *Itgal* (Fig. 4f, g). Neutrophil cluster (cluster 9) expressed *Ly6g*, *Cd177* and *Chil3*. Finally, we identified small cluster of contaminating fibroblasts (cluster 10), apoptotic cells (cluster 8) and proliferative cells (cluster 11) (Fig. 4f, g).

In the infection, relative cluster abundances were substantially altered (Fig. 4j), in concordance with flow cytometry data depicted above (Fig. 1g). Remarkably, while Mac clusters 1 and 2 were significantly reduced in infection, the IFN-associated Mac cluster (0) seemingly persisted under same conditions (Fig. 4j). However, RNA counts in cluster 0 from the infected animals were considerably lower compared to control conditions (Suppl. Fig. 4f), possibly pointing to cellular stress and transcriptional shut-down.

On the other hand, clusters 5 and 6 representing patrolling and classical *Ccr2, Ly6c*^{hi} monocytes, respectively, were enriched in the infection (Fig. 4j). However, an additional monocyte cluster (cluster 4) appeared in the infection that was virtually absent in the steady state (Fig. 4g, j). These „infection-associated monocytes" highly expressed *Nos2, Saa3, Ccl4, Ccl5, Cfb, Ass1* and *Slamf7*, in comparison to the classical monocytes (cluster 6) found in steady state, which expressed higher levels of *Vcan, Mmp8, Chil3, Sell,* and *Ifitm6* (Fig. 4m). Furthermore, GO term analysis revealed that classical monocytes (cluster 6) in the infection exhibited a strong defence response signature, while infection-associated monocytes (cluster 4) were enriched for genes associated with migration and adhesion (Fig. 4n). Together, these results revealed concurrent existence of two transcriptionally specific monocyte population, one of which emerges only in the infection and has a highly migratory phenotype.

In addition to the observed changes in the mononuclear myeloid compartment, other myeloid populations also underwent changes in the infection. In particular, we identified two distinct

neutrophil populations in infected mice, with „infection-associated neutrophils" (cluster 3) showing a more intermediate *Ly6g* expression compared to the cluster 9, but a higher *Clec4d, Cxcr4* and *Sell* expression (Fig. 4f, g).

Accordingly, although CNS myeloid cells were generally activated, monocytes were, together with neutrophils, the main drivers of inflammatory genes expression (Fig. 4m), indicating a crucial, and subset-specific role in promoting inflammation. Notably, while inf-associated neutrophils were the major cell type expressing *Il1b, Nlrp3, Isg15* and *Tnf* (Fig. 4m, Suppl.Fig. 4e), inf-associated monocytes from cluster 4 were the main drivers of *Ass1* and *Nos2* expression (Fig. 4m, Suppl.Fig. 4f).

Therefore, scRNA-seq analysis revealed a distinction between classical monocytes present in homeostatic dura compared to the ones appearing in the infection.

3.5 Skull marrow pool is insufficient in providing dural monocytes in the infection

Given the essential and complex role of monocyte subsets in infection, we next explored their origin. To understand the general functional role of monocytes in the dura under infection, we analysed *Ccr2*$^{-/-}$ mice, in which Ly6C^{hi} monocytes are unable to egress from the bone marrow. Comparison of CFU counts did not reveal differences in bacterial spread between infected *Wt* and *Ccr2*$^{-/-}$ mice in the periphery or the brain (Suppl. Fig. 5a), indicating that infiltrating monocytes *per se* were not involved in bacterial transfer across the brain barrier.

In accordance with previous reports, monocyte numbers in the dura in *Ccr2*$^{-/-}$ mice were comparable to monocyte numbers in *Wt* mice in steady state, (Fig. 5a)[37]. In contrast, unlike in *Wt* mice, we did not observe a significant monocyte influx in *Ccr2*$^{-/-}$ mice upon infection in the dura (Fig. 5a, Suppl. Fig 5b) or in the brain (Fig. 5b). This phenomenon was not compensated for by higher numbers of infiltrating granulocytes, as *Ccr2*$^{-/-}$ mice showed even lower neutrophil numbers in dura as compared to *Wt* mice during GBS infection (Suppl. Fig. 5b, c). Of note, Ly6C^{hi} classical monocytes in the dura expressed less *Ccr2* in steady state in comparison to monocytes isolated from blood or femur (Suppl. Fig. 5d).

Very recent reports have highlighted the skull marrow as the primary source for monocytes and B-cells replenishing the dura in homeostasis[12,38]. In order to revisit this finding and evaluate the contribution of the skull marrow as a hematopoietic hub during GBS infection, we performed bone marrow transplantations on head shielded or fully irradiated CD45.1 mice. First, we explored the source of monocytes in the dura in steady state. We then transferred bone marrow from either *Cx3cr1*$^{+/gfp}$ or *β-actin-GFP* mice. In both cases, monocytes (Fig. 5c) or DM (Fig. 5f) derived from the donor were GFP-labelled. In non-shielded irradiated mice, all

monocyte populations reached close to 100% chimerism after 8 weeks post transplantation (Fig. 5d). Femurs of head-shielded mice showed incomplete chimerism as previously reported[39], and significantly less contribution of donor-derived cells in the skull marrow, which was predominantly protected by head-shielding (Fig. 5d).

To understand similarities and differences between donor-cell integration dynamics in dura and bone marrow sites, we calculated relative chimerism rates by comparing the ratios of GFP-positive monocytes in dura and skull and femur bone marrow (Fig. 5e). In fully irradiated mice, there was no difference in monocyte populations at the three sites. In head-shielded mice, skull monocytes and dural monocytes had almost identical chimerism (Fig. 5e). In contrast, femur monocytes had almost two times higher replacement rate compared to dural monocytes (Fig. 5e). Considering the relatively short lifespan of Ly6C^{hi} monocytes[40], these results strongly suggest that the skull marrow exceeded peripheral bone marrow as monocyte reservoir in steady state.

Notably, whole body irradiation resulted in 70% DM replacement, while head-shielded mice had only a minor population of donor-derived DM (Fig. 5f). In line with our fate mapping results presented above, head shielded mice had a DM replacement of approximately 24% in 8 weeks after transplantation (Suppl. Fig. 4a). In addition and as reported before[39], irradiation let to a minor engraftment of donor-derived cells to the brain parenchyma (around 1.2%), which was further reduced in head shielded chimera (Suppl. Fig. 5f).

Next, to understand the anatomical source of the monocyte influx during infection, we infected head shielded chimeras 8 weeks after bone marrow transplantation with GBS (Fig. 5g). The chimerism in skull and femur monocytes did not change significantly between infected and non-infected mice. In contrast, the percentage of donor-derived monocytes in the dura was higher upon infection. While the chimerism in the brain in steady state couldn't be determined due to very low monocyte number in the parenchyma, infection-induced infiltrating monocytes showed a comparable chimerism to monocytes in the dura (Fig. 5h). Relative chimerism of monocytes in head shielded infected mice showed equal chimerism rates in femur and dura, while the chimerism in dura significantly exceeded that of skull monocytes (Fig. 5i). Accelerated replacement dynamics under infection indicate an extensive recruitment of monocytes from peripheral sources, without a preferential anatomical bone marrow niche. Additionally, the acceleration of DM replacement by donor-derived monocyte progenitors point to a faster monocyte-to-Mac differentiation in the acute infection (Fig. 5j). Together, these results indicate that the previously suggested CCR2-independent homeostatic replenishment of dura monocytes from the skull marrow does not suffice to meet the highly increased demand for monocytes in streptococcal meningoencephalitis.

3.6 GBS Infection changes monocyte precursors in the adjacent skull bone marrow

In view of the infiltration of monocytes from different bone marrow sources to the dura, it seemed essential to investigate monocyte differentiation patterns at the source sites. Previously, fate-mapping models showed that monocytes originate from granulocyte-monocyte progenitors (GMP)[41]. Yet, a small proportion can also stem from a GMP-independent source, most likely the monocyte-DC progenitor [MDP, Fig. 6a][42,43]. To explore the progenitor source of the extensive monocytic infiltration during GBS infection, we took advantage of *Ms4a3*$^{Cre/+}$*;R26*$^{Tomato/+}$ mice, where all GMP-derived cells are indefinitely labelled[42],nand analysed bone marrow from skull and femur of control and infected mice. In line with previous reports[44,45], we defined the monocyte progenitors (including both cMOP and iMOP) as CD45^{pos} CD11b^{neg} CD115^{hi} Ly6C^{pos} CD117^{lo-hi}, MDPs as CD45^{pos} CD11b^{neg} CD115^{hi} Ly6C^{neg} CD117^{hi}, while mature monocytes were CD45^{pos} CD11b^{hi} CD115^{hi} Ly6C^{pos} CD117^{neg} (Suppl. Fig. 6a). Tomato labelling was uniformly close to 100% in steady state in all analysed populations isolated from both skull or femur (except for MDP used as a negative control). However, Tomato-labelling markedly differed between marrow sites in infection: while labelling of skull monocytes was notably reduced during infection, the same was not observed in the femur bone marrow (Fig. 5b). This indicated a raise in a proportion of MDP-derived monocytes arising in the skull, but not in the femur marrow.

In the dura, 23.3±1.96% of DM were Tomato-positive in *Ms4a3*$^{Cre/+}$*;R26*$^{Tomato/+}$ mice in steady state at 8 weeks of age. This aligns with our earlier finding that within this timeframe, monocyte-driven DM turnover is 24%n(Fig. 4b). Based on turnover kinetics, this indicated that most monocyte-derived DM are originating from GMPs under homeostatic conditions (Fig. 6c, Suppl. Fig. 6b). The percentage of Tomato-labelled DM did not significantly decrease in infection (from 23.3±1.96% to 17.8±6%). Our results above, however, showed a dramatic increase in monocyte-derived DM upon infection, therefore it appeared that newly recruited DMs did not derive from GMP. We hence speculated that DMs were replenished by MDP-derived monocytes upon infection. Notably, labelling of monocytes in the dura and in the blood was also reduced under infection similarly to the skull, while neutrophil labelling remained the same (Fig. 6c, Suppl. Fig. 6d). This was in agreement with our hypothesis, as GMP are the only known neutrophil progenitor. Due to extremely low numbers of monocytes and neutrophils in the homeostatic brain parenchyma, labelling in steady state could not be determined. Under infection, however, the labelling of neutrophils in the brain was significantly higher than the labelling of monocytes, comparable to the situation observed in dura (Fig. 6d). Tomato-positive cells were observed mostly in the proximity of the leptomeninges (Suppl. Fig. 6c).

Next, we investigated if the observed phenomenon was due to emergency myelopoiesis, i.e. if the MDP-derived monocyte production was increased since GMP progeny output did not suffice to meet the high demands of monocytes in meninges and the brain in infection. The monocyte population in skull and femur was slightly increased in proportion after the infection (Fig. 6e). Nonetheless, the infection led to a drastic decrease of monocyte progenitors (MP), including cMOP and iMOP, as well as MDP in the skull (Fig. 6f, g, Suppl. Fig. 6a). A similar, but less pronounced pattern was observed in the bone marrow of the femur (Fig. 6f,g).

In addition, the small remaining MP population in both skull and femur bone marrow showed a more immature state, with lower expression of *Cd115*, *Itgam*, and *Cd74,* while *Ms4a3* was upregulated (Fig. 6h).

Together, we showed that during acute GBS infection, accelerated monocyte differentiation to DM is likely MDP-driven. We were speculating that this might be a compensatory mechanism due to over-utilization of GMP for neutrophil production in the infection, leading to a lack of available differentiated monocyte progenitors. In order to explore, if monocyte progenitors from an uninfected donor could help replenishing the niche, we adoptively transferred 2-4x10^5 lineage committed MP from *β-actin-GFP* mice (procedure as depicted in Suppl. Fig. 6d) i.v. into mice 1 dpi (Fig. 6i). We found the majority of GFP^+ cells that localized to the infected dura upregulated CD11b (Fig. 6j-k), and around 20% were $Ly6C^+CD206^{pos}$ (Fig. 6l). On the other hand, almost no adoptively transferred GFP^+ cells were found in the dura of control mice (Fig. 6j) in this short timeframe. Therefore, it seems that in the infected dura both GMP-derived and MDP-derived monocytes can be utilized for differentiation into DM, depending on the progenitor availability and “openness” of the niche. Taken together, these results demonstrate an impressive differentiation plasticity of monocytes to meet conflicting, desease-dependent requirements in the CNS. Furthermore, they point to the cranial marrow as an important source of DM, especially under homeostatic conditions, and to the peripheral bone marrow and MDP progeny as a last resort for monocytes in extreme infection situations to accelerate replenishment of DM by monocyte-derived Macs

4. Discussion

While the majority of the neuroimmune studies over the years focused on MG as a main cellular component of CNS defence, a growing body of evidence show Macs residing in brain barriers, particularly meninges, play important roles in different neuropathologies[4,5,46]. Additionally, recent findings highlighting a direct communication between the dura mater and

skull marrow attract questions about the dynamics of indicated hematopoietic hub in disease [11–13,47]. Here, we focus on Macs in different CNS niches during an acute phase of streptococcal meningoencephalitis, and using different fate-mapping tools, follow their immune response. In line with that, we show that in steady state, dural Macs are already immunologically ”primed” compared to MG, with higher expression of genes related to defence responses, likely due to their specific position at the crossroads of the neuroimmune interface[10]. In the infection, meninges limit bacterial dissemination towards the parenchyma. However, MG activation is already detectable on subtle levels with morphological adjustments dependent on the bacterial load in the brain. It is conceivable that morphological changes are region-specific, with brain regions containing MG in contact or closer proximity to the leptomeninges being more affected. If MG activation is essential to restrict GBS spread upon overcoming the meningeal barriers to the brain parenchyma or if this activation is only secondary, would need to be further evaluated. Spatial RNA sequencing might offer more insight in the future in discrete MG signatures dependent on the association with the bacteria.

Unlike most of the CAMs, DM are replenished to a higher percentage by monocytes during steady state. We followed the kinetics of this differentiation using a *Cxcr4*^{CreER} fate-mapping model, and showed a steady linear curve concluding in around 50% DM replacement in 4 months. These dynamics swiftly changed in the infection, characterized by the disappearance of resident DM and more rapid differentiation of incoming monocytes into the resident DM-like CD206^{+} population. Additionally, an appearance of a Ly6C^{+}CD206^{+}MHC-II^{+} “immature“ Mac population was observed, which is typically not discernible in steady state. This Mac population, however, was not identifiable as a specific cluster in scRNA-seq data from infected mice, likely due to its transient nature and discrepancy between surface markers and transcriptome expression. The scRNA-seq of the myeloid cells isolated from dura revealed heterogeneity of Mac, which separated into three distinct clusters. Two clusters exhibited diminution in the infection, while the cluster 0, defined by its enrichment in expression of type I IFN genes, persisted but showed signs of cellular stress. It is possible that these resident DM populations are the first responders early in the infection leading to cellular stress and ultimately, cell death. This observation was in line with the so-called Mac disappearance reaction” which has been described under inflammation in the peritoneal cavity[48,49], liver[50] and other tissues[51] and which might serve to initiate infection control[48]. Infection-regulated cell death of resident Macs has also been found in the meninges in viral infection[4], accompanied by the engraftment of monocytes.

The skull bone marrow can act as a reservoir of myeloid cells, directly supplying the dural environment with monocytes[12]. This finding is especially interesting in the context of

meningoencephalitis, in which an extensive need for monocytes arises, not only for the induction of inflammatory responses, but also to serve as a potential Mac precursors in an empty niche. Indeed, while homeostatic dura hosts classical and non-classical monocytes, a substantial expansion was observed in the infection, with a significant influx of transcriptionally distinct infection-associated monocytes. Additionally, we show that while steady state dura can be replenished by monocytes in CCR2-independent way, *Ccr2*$^{-/-}$ mice exhibit an absence of monocyte influx into the dura under infection. Of note, we did not find evidence that these infection-associated monocytes contribute to bacterial trafficking, as *Ccr2*$^{-/-}$ mice did not have a difference in bacterial burden compared to *Wt* animals. This goes in hand with studies identifying numerous genes in GBS responsible for facilitating the adhesion of the bacteria to the endothelium, enabling transcytosis as a method of crossing the CNS barriers[18,52,53].

By using head-shielded bone marrow chimeras, we corroborate the finding that the skull marrow provides the adjacent dura with monocytes during steady state. Remarkably, head-shielded mice had only less than 8% of donor-originating DM, while our fate-mapping experiments revealed that in the timeframe of 8 weeks monocyte replacement would reach around 24%. These results point to the skull marrow as a homeostastic source for monocytes to engraft in the niche and replace DM from prenatal sources. Infection, however, disrupts these homeostatic routes of monocyte egress and differentiation. In infected head-shielded mice, chimerism rates were significantly higher in dura and brain, further driving the point that skull marrow cannot sufficiently provide for high monocyte requirement in meningoencephalitis and other hematopoietic progenitor sources are needed. This observed „recruitment threshold“ during infection entails changes in the skull marrow composition, especially in monocytes and monocyte precursors, including cMOP, iMOP and MDP. Detected presence of GBS in the skull marrow implies the instigation of emergency hematopoietic programs. Indeed, our data support this shift in myelopoiesis, with the MDP and MP population being significantly decreased. Additionally, remaining MP changed their gene expression, downregulating typical MP and monocyte genes while upregulating canonical GMP gene *Ms4a3*. Together these results indicate a faster recruitment and differentiation, leading to less progenitors in the marrow left, with a less differentiated transcriptional phenotype. While we show that in steady state, monocytes and monocyte-derived Mac in dura are GMP-derived, in infection an MDP-derived monocyte population arises in skull marrow and dura. Interestingly, a recent report identified *Sell* and *Slamf7* as discriminatory markers for monocytes derived from GMP or MDP, respectively[43]. Indeed, our single-cell transcriptomic profiling showed upregulation of *Sell* in homeostatic population of dural monocytes, while infection-associated monocytes upregulated *Slamf7,* indicating their possible MDP origin. Therefore, infection-induced accelerated monocyte influx into the myeloid compartment of dura and brain seems

to be dependent on the possible existence of discrete molecular mechanisms regulating a differentiation trajectory of monocytes from GMP or MDP origin. The precise contribution and disease implication of this diverted differentiation, as well as the precise anatomical source of monocyte progenitors from the skull, femur or blood remains to be resolved.

Taken together, we integrated fate mapping approaches and transcriptomic data to elucidate underdefined immune processes happening in distinct brain niches by discrete Macs and monocyte subsets. In conclusion, streptococcal meningoencephalitis led to reciprocal changes in monocyte and Mac lineage of the skull marrow and dura and altered monocyte-to-Mac differentiation dynamics, likely driven by the inflammatory-related Mac disappearance.

5. Acknowledgements

We thank Anita Imm, Reem Alsumati, Adriana Greco and Lena Grubišić for their great technical assistance. We thank the ZTZ core facility, especially Jan Bodinek and Marie Follo for their great technical assistance. We thank Pedro Aniceto for his assistance with analysis in R and R Studio.

6. Author contribution

PH and VG conceptualized the study and wrote the manuscript. VG preformed and analysed most of the experiments. FL preformed the analysis of the scRNA-seq data. VF preformed the wet-lab part of the 10X Genomics scRNA-seq experiments. LFPB performed morphometric reconstruction of microglia. JN and ZMM helped with irradiation and other experiments. TM and JH helped with the experiments. AL and JK helped with experiments and provided relevant intellectual input. SB and MF provided relevant intellectual input. KK and DE provided significant intellectual input and DE helped with single-cell sequencing experiment.

7. Declaration of interests

The authors have no competing interests to declare.

Figure legends

Figure 1: Haematogenous spread of GBS causes rapid brain inflammation

a: Colony forming units (CFU) counts from homogenized brains (n=25), dura (n=21), liver (n=16), extracted bone marrow from femur (n=19) and skull (n=25) and blood culture (per ml) (n=24) at 2 dpi. Data represent at least five independent experiments. Mean ± SEM is shown.

b: Representative maximal intensity projection of sagittal brain slices of infected *Cx3cr1*$^{gfp/+}$ mice including leptomeningeal area and parenchyma stained with GBS-AF633 (magenta) and DAPI (blue). White and magenta arrows mark some of the GBS found in the parenchyma. Scale bar = 50 µm.

c: Fluorescence intensity of GBS-AF633 staining divided with the area of leptomeninges or cortex. Each dot represents an individual infected mouse, n=8. Statistics by paired t-test. **p<0.01, data represents at least two independent experiments.

d: Representative maximal intensity projection of dural whole mount from infected *Cx3cr1*$^{gfp/+}$ mice stained with DAPI and GBS-AF633. SS = superior sagittal sinus, TS = transverse sinus. Scale bar=50 µm, if not stated otherwise. Illustrative representation of dura made with BioRender (biorender.com).

e: Absolute numbers of microglia (MG), monocytes (Monos), neutrophils (Neutros) and CNS-associated Macs (CAM), including leptomeningeal, perivascular and choroid plexus Macs from control (yellow bars, circles) and infected (purple bars, squares) mice measured by flow cytometry. One brain hemisphere per mouse was used for quantification, but the brain was not dissected further. n= 5-7, data represents at least two independent experiments. Mean ± SEM is shown. Multiple Mann-Whitney test followed by Holm-Šídák, *p<0.02, ns = not significant

f: Correlation of CFU counts and total monocyte (pink) or neutrophil number (purple) in the brain measured by Spearman correlation. Slopes compared by simple linear regression, n=20. Data represent at least three independent experiments. R represents the goodness of fit in simple linear regression. p<0.0001

g: Absolute numbers of monocytes (Monos), neurtrophils (Neutros) and dural macrophages (DM) from control (yellow bars, circles) and infected (purple bars, squares) dura mater measured by flow cytometry, n=6-7. Cranial dura was extracted as described in method section and quantified. Mean ± SEM is shown. Statistics by Multiple Mann-Whitney test

followed by Holm-Šídák. Data represent at least two independent experiments. *p<0.05, **p <0.002

h: Representative maximal intensity projection of dural whole mount from control and infected *Cx3cr1*$^{gfp/+}$ mice stained with DAPI and GBS-AF633 showing loss of GFP-positive macrophages. Full arrows indicate neutrophils, while hollow arrows point to monocytes. Scale bar = 20 µm

Figure 2: MG and DM share a type-I interferon response to GBS infection

a: Schematic representation of experimental time course. *Mrc1*$^{CreER/CreER}$*;R26*$^{Tom/Tom}$ mice were treated with tamoxifen twice, 8 weeks prior to the infection. At 2 dpi, DM and MG were sorted from dura and brain. Two mice were pooled for n=1, in total 6 mice were used (n=3).

b-c: Gating used for FACS from dural Macs (DM) (**b**) and MG from the brain (**c**) from *Mrc1*$^{CreER/CreER}$*;R26*$^{Tom/Tom}$ mice induced with TAM for 8 weeks before the infection.

d: Principal component analysis (PCA) of sorted populations.

e: Z-score heat map of 93 common upregulated DEG in both MG and DM, with log2fold change larger than 1.5.

f: Normalised counts of selected genes from RNA sequencing. Statistics done by one-way ANOVA followed by Tukey's test. n=3, data are mean ± SEM. **p<0.01, ***p<0.001, ****p<0.0001

g-h: p:Profiler Gene Ontology analysis of genes that were upregulated only in DM **(g)** or only in MG **(h)** of infected mice. Only top 7 GO Terms were depicted.

i: Normalised counts of selected genes from steady state DM and MG. Statistics done by unpaired t-test. Data are mean ± SEM, n=3, ***p<0.001, ****p<0.0001

Figure 3: MG responses to the infection are dependent on association with bacteria

a: FACS sorted MG expression of *Tnf-α*, *Il-1β*, *Ccl2* and *Cxcl1* measured by qRT-PCR and plotted against bacterial burden in the brain. n=7, correlation measured by Spearman r, p and r values indicated on the graphs.

b: Bar chart representing different groups of disease severity depending on the bacterial burden in the brain. n=3 for Ctrl and Moderate, n=4 for High.

c: Representative pipeline of 3DMorph MG annotation and analysis. Scale bar = 50 µm

d-g: Cell volume, ramification index, cell territory volume and average branch length in MG of mice with different disease severities. Statistics by one-way ANOVA nad Tukey's multiple comparisons test. Number of cells analysed, for Ctr=842, for Moderate=1396, for High=2026. Number of mice n=3 for Ctrl and Moderate, n=4 for High. Data are mean ± SEM, *p<0.05,***p<0.001, ****p<0.0001, ns=not significant.

h: Representative confocal image of infected brain from *Cx3Cr1*$^{gfp/+}$ mice. Full arrow indicates a MG cell in proximity of the bacterial clusters in leptomeninges, hollow arrow indicates to a MG cells on a more distal site. Scale bar = 20 µm

i: Comparison of cell volume and ramification index of MG from the infected mice. “Proximal” indicates cells that are up to 140 µm away from the leptomeninges, “distal” cells include the ones more further than 140 µm. n(mice)=3, n(cells)=23-25 for ctrl, 39-42 for inf. Data are mean ± SEM, Statistics by ordinary one-way ANOVA, followed by Tukey's multiple comparisons test. *p<0.05,**p<0.01,***p<0.001, ns=not significant.

Figure 4: Increased diversity of dural myeloid cells in infection

a: Schematic representation of experimental timeline. *Cxcr4*$^{CreER/+;}$*R26*$^{Tom/Tom}$ mice were induced for 8 weeks before GBS infection and sacrificed at 2 dpi.

b: Percentages of labelled CD206-positive cells (DM) in dura and CD45^{lo}CD11b^{+}Ly6C^{neg}Ly6G^{neg}CD206^{neg} cells (MG) in brain. Data are mean ± SEM. Statistic by Mann-Whitney U-test n=4-5. Data represent three independent experiments. *p<0.05, ns=not significant.

c: Representative flow cytometry plots showing a presence of Ly6C^{hi}CD206^{+} population in infected and control mice. Numbers in each gate indicate the percentage of the population.

d: Flow cytometry-based quantification of Ly6C^{hi}CD206^{+} population in Ctrl and Inf mice, n=7 Data are mean ± SEM. Statistics by Mann-Whitney U-test. Data represent three independent experiments. **p<0.01

e: MHC-II expression in Ly6C^{hi}CD206^{+} population in comparison to Ly6C^{hi}CD206^{neg} monocytes and Ly6C^{neg}CD206^{+} DM. MHC-II expression is expressed as mean intensity fluorescence (MFI). Data are mean ± SEM. n=7, representing three independent experiments. Statistics by ordinary one-way ANOVA, followed by Dunnett's multiple comparisons test. *p<0.05, ***p<0.001

f: Uniform Manifold Approximation and Projection (UMAP) representation based on gene expression profiling of sorted CD45^{+}CD11b^{+} myeloid population from the control and infected dura of the *Wt* mice. Clustering was done using Seurat. 6 control and 5 infected mice were integrated via the sctransform algorithm.

g: Dotplot representing some of the canonical discriminatory markers of each identified clusters in steady state. Color represents the mean expression of the gene and the dot size represents the percentage of the cells expressing the gene in each cluster.

h-i: Volcano plots showing differentially expressed genes between IFN-associated DM and DM2 (**h**) and IFN-associated DM and MHC-II high DM (**i**) in steady state. Dotted lines represent a log2fold change cut-off of -1 and 1.

j: Relative abundance of clusters compared between control and infected mice. Statistics done by two-way ANOVA followed by Bonferroni's multiple comparisons test. Data are mean ± SEM, ***p<0.001, ****p<0.000, ns=not significant.

k: Volcano plot representing differentially expressed genes in two different monocyte cluster, with cluster 6 on the left and cluster 4 on the right. Dotted lines represent a log2(fold change) cut-off of 1 and -1.

l: Top five GO Terms enriched in cluster 6 on the left and cluster 4 on the right.

m: Dotplot representing some of the canonical inflammatory genes in the infection. Color represents the mean expression of the gene and the dot size represents the percentage of the cells expressing the gene in each cluster.

Figure 5: Skull marrow pool is insufficient in providing dural monocytes in the infection

a: Flow cytometry quantitative analysis of monocytes from dura of control and infected *Wt* or *Ccr2*$^{-/-}$ mice. Whole cranial dura was processed and absolute numbers were plotted. n=7-10, data are mean ± SEM, statistics by one-way ANOVA and Bonferroni's multiple comparisons test **p<0.01, ***p<0.001, ns=not significant.

b: Flow cytometry analysis of monocyte frequencies from the brains of control and infected *Wt* or *Ccr2*$^{-/-}$ mice. n=4-7, data are mean ± SEM, statistics by one-way ANOVA and Bonferroni's multiple comparisons test, *p<0.05, **p<0.01, ns=not significant.

c: Schematic representation of different strategies of radiation procedure followed by bone marrow transplantation from *Cx3cr1*$^{+/gfp}$ or *β-actin-GFP* mice. Analysis was done after 8 weeks. Representative flow cytometry plots depicting donor-originating monocytes in green, from either fully irradiated mice or head-shielded mice. Numbers in gates represent % of gated GFP-positive (donor-derived) cells.

d: Chimerism rates in monocytes from skull or femur after either full irradiation or head-shielding. Data represents three independent experiments, n=7. Data are mean ± SEM, statistics by two-way ANOVA and Tukey's multiple comparisons test, *p<0.05, ****p<0.0001, ns=not significant. Illustration made in BioRender (biorender.com).

e: Chimerism rates of monocytes in dura compared to chimerism of skull monocytes, or femur monocytes, with depicted formula. Statistics by two-way ANOVA followed by Tukey's multiple comparisons test. n=7, data represent three independent experiments. Data are mean ± SEM, ***p<0.001, ****p<0.0001, ns=not significant.

f: Chimerism rates of DM in fully irradiated or head-shielded mice. Statistics by Mann-Whitney U – test. n=7, data represent three independent experiments. Data are mean ± SEM, ****p<0.0001.

g: Schematic representation of experimental timeline post head-shielded irradiation. 8 weeks post head-shielded irradiation and bone marrow transfer, mice were infected with GBS and analysed 2 dpi.

h: : Chimerism of monocytes in skull, femur, dura and brain of control and infected head-shielded chimeral. Two-way ANOVA followed by Šídák's multiple comparisons test, n=5-7, from two independent experiments. Data are mean ± SEM. *p< 0.05, ns = not significant.

i: Chimerism rates of monocytes in dura compared to chimerism of skull monocytes, or femur monocytes, in control or infected head shielded mice. Data are mean ± SEM, n=5-7 from two independent experiments. Statistics by unpaired multiple t-test followed by the Holm-Šídák, *p<0.05.

j: Chimerism of DM post infection measured by flow cytometry. Statistics by unpaired t-test. n=5-7, from two independent experiments. *****p< 0.05

Figure 6: GBS Infection changes monocyte precursors in the adjacent skull bone marrow

a: Schematic representation of either GMP or MDP-derived monocyte lineages and percentages of Tomato-positive cMOP, iMOP and MDP in *Ms4a3*$^{Cre/+}$*;R26*$^{Tomato/+}$ mice in skull and femur, in steady state or 2 dpi. Data are mean ± SEM, n=4-5, from two independent experiments. Statistics by two-way ANOVA and Tukey's multiple comparisons test. ns=not significant.

b: Percentages of Tomato-positive monocytes in *Ms4a3*$^{Cre/+}$*;R26*$^{Tomato/+}$ mice in skull and femur, in steady state or 2 dpi. n=4-5, from two independent experiments. Data are mean ± SEM. Statistics by one-way ANOVA and Tukey's multiple comparisons test. ****p<0.0001, ns=not significant

c-d: Percentage of Tomato-positive cells from dura (**c**) and brain (**d**) 2 dpi. Due to negligably small number of monos and neutros in the brain in steady state (less than 100), percentage is marked as n.d.= non-detectable. Data are mean ± SEM. Statistics by multiple unpaired t-test, n=4-5 from two independent experiments. ns = not significant, **p < 0.01, ****p<0.0001.

e: Relative fractions of monocytes of femur or skull marrow in steady state and infection expressed as % of total CD45^{+} cells. Data are mean ± SEM. Statistics by multiple Mann-Whitney test followed by the Holm-Šídák, n=9, data represents at least three independent experiments. ns = not significant, *p < 0.05.

f: Relative fractions of MDPs of femur or skull marrow in steady state and infection expressed as % of total CD45^{+} cells. Data are mean ± SEM. Statistics by multiple Mann-Whitney test followed by the Holm-Šídák, n=4, data represents two independent experiments. ns = not significant, ***p < 0.001.

g: Relative fractions of MP (including cMOP and iMOP) of femur or skull marrow in steady state and infection expressed as % of total CD45^{+} cells. Data are mean ± SEM. Statistics by multiple Mann-Whitney test followed by the Holm-Šídák, n=9, data represents three independent experiments. ns = not significant, ***p < 0.001.

h: Expression of *CD115*, *Itgam*, *Ms4a3* and *Cd74* measured by qPCR from sorted monocyte progenitors from bone marrow of femur and skull. Data are mean ± SEM. Statistics by multiple Mann-Whitney test followed by the Holm-Šídák, n=6. Data represent two independent experiments. *p < 0.05

i: Schematic representation of experimental setup for adoptive transfer experiment. *Wt* mice were infected and 1 dpi received 2-4x10^5 monocyte progenitors sorted from bone marrows of *β-actin-GFP* mice. Control mice were administered with PBS before receiving transferred monocyte progenitors.

j: Flow cytometry plots representing gating strategy and GFP^+, donor derived cells in dura of the control and infected mice.

k: Graph showing upregulation of CD11b in most of the donor-derived GFP^+ cells found in the dura of infected mice. Data are mean ± SEM and represent three independent experiments. n=6

l: Graph representing percentages of cells upregulating CD206 and Ly6C out of the $CD11b^+GFP^+$ cells found in the dura of infected mice, n=6. Data represent three independent experiments. Data are mean ± SEM.

Suppl. Figure 1: a: Weight loss curve in the first three days of the infection, for 1 dpi n=20, for 2 dpi n=23 and for 3 dpi n=8. Data are mean ± SEM.

b: ELISA of plasma 2 dpi, n=5. Statistics by Mann-Whitney U-test. Data represents 2 independent experiments**.** Data are mean ± SEM. **p< 0.01

c: TNF-α, IL-1β and IFN-β ELISA from homogenized brains. Measured values are normalized with the brain mass in mg. For IFN-β n=7, TNF-α and IL-1β n=11. Data represent at least three independent experiments. Data are mean ± SEM, **p< 0.01, p****<0.0001

d-e: Representative flow cytometry plots of percentage of monocytes and neutrophils in infected (**d**) brain or (**e**) dura. Numbers indicate percentages of the population, out of all myeloid cells.

Suppl. Figure 2: a-b: Maximum intensity projection of dural whole mount (**a**) and brain sagittal sections (**b**) from *Mrc1*$^{CreER/CreER}$;*R26*$^{Tom/Tom}$ mice. In **a**, Tomato signal co-localizes with DM stained with CD206 antibody. In **b**, MG do not express Tomato signal, while perivascular and leptomeningeal MΦ (marked by white arrows) do. Scale bar = 50 µm

c: Volcano plots indicating fold changes (log2) and padj values (−log10) of genes expressed in steady state DM and MG. Yellow and blue dots represent some of the differentially expressed signature genes in DM and MG, respectively.

d-e: Gene Ontology analysis of genes upregulated in steady state DM (**d**) compared to steady state MG and vice versa (**e**), respectively.

Suppl. Figure 3: a: Representative maximum intensity projections from infected brain indicating the distance from the leptomeninges. MG was stained with Iba-1-AF633. Scale bar = 50 µm.

b: Representative 3DMorph reconstruction of image from **a**. White arrow marks a skeletonized cell used as an example.

Suppl. Figure 4: a: *Cxcr4*$^{CreER/+;}$*R26*$^{Tomato/Tomato}$ mice were induced for 3 days, 1,8 or 16 weeks, recombination in DM and MG was measured as a percentage of Tomato positive CD45^{hi}CD11b^{+}Ly6G^{neg}CD206^{+} DM in dura or CD45^{lo}CD11b^{+}Ly6C^{neg}Ly6G^{neg}CD206^{neg} MG in parenchyma.

b: In *Cxcr4*$^{CreER/+;}$*R26*$^{Tomato/Tomato}$ mice, more than 80% of Ly6C^{hi}CD206^{+} population expresses Cxcr4 (and is Tomato positive), both in control and infected group. Data are mean ± SEM, n=4 Statistics by Mann-Whitney U-test. Data represent two independent experiments.

c: Dotplot representing some of the canonical discriminatory markers of each identified clusters in infection. Color represents the mean expression of the gene and the dot size represents the percentage of the cells expressing the gene in each cluster.

d: RNA counts across the clusters in control and infected samples.

e-f: Feature UMAPs showing expression of *Il1β, Nlrp3, Isg15*, *Tnf* (**e**) and *Nos2* and *Ass1* (**f**) in control clusters (on the left) and infected clusters (on the right) showing their high expression in infection in monocyte and neutrophil-associated clusters.

Suppl. Figure 5: **a:** CFU counts from blood, spleen and brain of infected *Wt* or *Ccr2*$^{-/-}$ *mice*, n=7-12, statistics by multiple U-tests followed by Holm-Šídák, data are mean ± SEM and represent at least three independent experiments. ns= not significant.

b: Frequencies of monocytes, neutrophils and DM indicated as percentages of CD45-positive cells in dura of *Wt* or *Cct2*$^{-/-}$ mice. n=6-10, data are mean ± SEM and represent at least three independent experiments

c: Flow cytometry analysis of neutrophils in dura of control and infected *Wt* or *Cct2*$^{-/-}$ mice. Statistics by one-way ANOVA and Bonferroni's multiple comparisons test (n=7-9). Data are mean ± SEM and represent at least three independent experiments. *p<0.05

d: *Ccr2* expression measured by qPCR from monocytes sorted from blood, femur, skull and dura (n=6) of *Wt* mice. Data are mean ± SEM. Statistics by Kruskal–Wallis one-way analysis of variance. *p<0.05

e: Chimerism percentages of MG from fully irradiated or head shielded mice, n=3-5, Mann-Whitney U-test. Data are mean ± SEM. ***p<0.001

Suppl. Figure 6: a: Flow cytometry plots representing the gating strategy of monocytes (monos), monocyte progenitors (MP) and MDPs from the skull bone marrow of the control and infected mice.

b: Maximum intensity projection of whole-mount dura from steady-state *Ms4a3*$^{Cre/+}$*;R26*$^{Tomato/+}$ mice showing co-localization of Tomato signal with CD206, indicating DM in dura differentiating from GMP-derived monocytes. Scale bar = 50 µm

c: Maximum intensity projection of sagittal brain slices from control and infected *Ms4a3*$^{Cre/+}$*;R26*$^{Tomato/+}$ mice showing an increase in Tomato signal in leptomeningeal area post infection. Scale bar = 50 µm

d: Flow cytometry analysis of blood from control and infected *Ms4a3*$^{Cre/+}$*;R26*$^{Tomato/+}$ mice, populations are expressed as a percentage of CD45^{+}CD11b^{+} cells. n=4-5, statistics by two-way ANOVA, followed by Bonferroni's multiple comparison test. Data are from two independent experiments and are mean ± SEM. ns = not significant, ***p<0.001

e: Gating strategy used to sort monocyte progenitors (MP) from *β-actin-GFP* mice.

5. Materials and methods

1. Mice

Both female and male mice from C57BL/6 genetic background were used at 6 to 12 weeks of age. C57BL/6J and C57BL/6N mice were purchased from Jackson Laboratories (USA) or Charles River Laboratories (Germany) and bred in the local animal facility. CD45.1-mice (B6.SJL-Ptprca Pepcb/BoyJ) were purchesed from Jackson Laboratories. *Cx3cr1*$^{gfp/+}$ mice were obtained as a kind gift from Steffen Jung (Weizmann Institute, Israel). *β-actin gfp+/− (C57BL/6-Tg(CAG-EGFP)131Osb/LeySopJ)* were purchased from Jackson Laboratories (USA). *Ms4a3*^{Cre} (C57BL/6J-Ms4a3em2(cre)Fgnx/J) mice were purchased from Jackson Laboratories. *Mrc1*^{CreER}*;R26*^{Tomato} mice were provided by Marco Prinz (Institute of Neuropathology, Freiburg) as a kind gift. *Cxcr4*^{CreER} mice were provided by Ralf Stumm (Neuropharmacology, Jena) as a kind gift.

Ccr2$^{-/-}$ (B6.129S4-Ccr2tm1Ifc/J) mice were bought from Jackson Laboratories (USA).

Mice were bred in animal facilities of the University of Freiburg under specific pathogen-free conditions and were kept in groups of a maximum of five animals per cage at a room temperature of 21 °C (±0.5–1 °C) and a humidity of 55% (±5–8%). Food and water were available ad libitum, and day/night cycles were set to 12 h. All animal experiments were approved by the Federal Ministry for Nature, Environment and Consumer's protection of the state of Baden-Wuerttemberg (proposal numbers G-19/031 and G23/008).

2. Mouse interventions

Induction of Cre recombinase by tamoxifen has been explained previously[34]. Briefly, mice were anesthetized by isoflurane inhalation. 4mg TAM in 200µl corn oil (both Sigma) was injected subcutaneously in *Cxcr4*^{CreER} or *Mrc1*^{CreER} mice at two time points 48h apart. As control, littermates with respective floxed alleles, but without Cre recombinase expression, were treated in the same fashion.

For bone marrow transplantations, recipient mice were anesthetized using ketamine (100 mg/kg body weight) and xylazine (10 mg/kg body weight) administered intraperitoneally.

Mice were then head-shielded with a 6mm lead plate, or not shielded and lethally irradiated with 9 Gy. Subsequently, mice received $5x10^6$ donor-derived bone marrow cells intravenously. Mice were analysed 8 weeks post transplantation.

3. GBS culturing and infection

Prior to infection, GBS strain BM110 was streaked on a blood agar plate (Columbia agar + 5% sheep blood; BioMérieux) and incubated at 37°C overnight. One colony from the blood agar plate was transferred into 5 ml of Todd-Hewitt broth and incubated at 37°C overnight. The overnight culture was inoculated into 200 ml warm Todd-Hewitt broth. Bacteria were grown to the mid-log phase, and bacterial concentration was determined with an optical spectrophotometer (OD600 = 0.4) and confirmed by serial dilutions plating onto a blood agar plate. Afterwards, bacteria were washed twice with PBS and resuspended in PBS at 10^9 CFU/ml. A total of 50 µl (5 x 10^7 CFU) suspension of bacteria or vehicle (PBS) was injected into the retro-orbital venous plexus. For this procedure, mice were anesthetised by isofluran inhalation.

4. CFU assay

Mice were sacrificed by CO_2 inhalation after which the blood was drawn from the heart. Mice were then transcardially perfused with ice-cold sterile PBS. Liver, spleen and brain were collected into sterile plastic bags, and mechanically dissociated. Femur was flushed through a 70 µm cell strainer using 2.5-3 ml sterile PBS in the syringe, and 20 µl of suspension was plated on Granada agar (BD). Skull marrow was extracted as previously described[12], with small modifications. After the removal of dura, the calvarium was cut into small pieces into 1 ml sterile PBS using sterile scissors and plated on Granada agar. Dura was incubated for 20 min at 37°C with shaking in 1 ml of sterile RPMI containing 2.5 mg of Collagenase IV after which 20 µl of suspension or serial dilution was plated on the Granada agar. To control sterility of the CFU assay, tissues of the control animals were plated in parallel, with no bacterial growth from any analysed organ.

5. Cell extraction:

Blood was drawn from the heart. Erythrocytes were lyzed in RBC Lysis buffer solution (eBioscience™ 1X RBC Lysis Buffer). The remaining cells were washed in FACS buffer (PBS + 1% FBS + 2 mM EDTA).

Dura mater was peeled using forceps from calvaria and placed into a digestion solution (2.5 mg/ml collagenase IV in RPMI) and incubated for 20 min at 37°C shaking, after which the solution was filtered through 70 µm strainer (BD) and washed with FACS buffer.

The remaining calvaria was cleaned from leftover muscle and fascia, placed into a 2 ml Eppendorf tube with 1 ml PBS and diced with scissors. The bone marrow was filtered through a 70 µm strainer and washed with FACS buffer.

Femur was cleaned from the leftover muscle, and the bone marrow was flushed with PBS using a 26G needle through a 70 µm strainer.

Brain was homogenized and filtered through a 100 µm strainer. Myelin was removed using 37% Percoll gradient and centrifugation for 30min at 300g RT, with no acceleration and brake.

Samples were washed and stained with respective antibodies. FcγII/III receptors were blocked by prior 10 min incubation with Fc block (anti mouse CD16/32 antibody Clone 93, Biolegend) on ice.

Samples used for bulk RNA-seq (dura and brain) were processed in the same way to avoid potential bias of Mac activation due to enzymatic digestion. Shortly, brain and dura were incubated for 20 min at 37°C shanking in 2.5 mg/ml collagenase IV, after which they were filtered through 70 µm strainer and washed with PBS. The pellet was resuspended using 37% Percoll and centrifuged for 30 min at 300g RT, without the acceleration and brake.

6. Flow cytometry and FACS

Cells were stained with the indicated antibodies according to manufacturer's instructions. Flow cytometry was performed on a 10-color flow cytometer Gallios™ (Beckman Coulter) and FACS was done on Moflo™ (Beckmann Coulter) or CytoFlex™ (Beckman Coulter).

The following anti-mouse antibodies were used for surface staining:

anti-mouse CD45 eFluor450 Clone 30-F11 (eBioscience),

anti-mouse CD45 FITC Clone 30-F11 (eBioscience)

anti-mouse CD45.1 FITC Clone A20 (eBioscience)

anti mouse CD45.2 PerCP Cy5.5 Clone 104 (eBioscience)

anti-mouse CD11b PE-Cy7 Clone M1/70 (eBioscience)

anti-mouse CD11b APC-eFlour780 Clone M1/70 (eBioscience)

anti-mouse CD117 PE Cy7 Clone 2B8 (eBioscience)

anti-mouse CD115 APC Clone AFS98 (Miltenyi)

anti-mouse CD115 BV421 Clone AFS98 (BioLegend)

anti-mouse CD206 PE Clone C068C2 (BioLegend)

anti-mouse CD206 AF488 Clone C068C2 (BioLegend)

anti-mouse Ly6G FITC Clone 1A8 (BD Pharmingen)

anti-mouse Ly6G APC Clone 1A8 (BD Pharmingen)

anti-mouse Ly6C BV605 Clone HK1.4 (BioLegend)
anti-mouse MHC II APC eFlour780 Clone M5/114.15.2 (eBioscience)

Analysis was done using Kaluza software (v1.5a and 2.1, Beckman Coulter).

7. Adoptive transfer of monocyte progenitors

Bone marrow was isolated from tibia and femur of *β-actin-gfp*$^{+/-}$ mice, flushed with sterile ice-cold PBS and centrifuged for 6 min at 1500 rpm. Cells were resuspended in 1% BSA in PBS, and then stained and sorted as described above. Sorted monocyte progenitors were then resuspended in PBS + 2% murine serum which was obtained from the donor mice. Monocyte progenitors were injected intravenously at 1 dpi (~2–4 × 10^5/animal). Recipients were analysed 1 day post transfer (2 days post infection). Blood, brain, dura and bone marrow (from femur and skull) were analyzed on a flow cytometer (Gallios™, Beckman Coulter) and processed with the Kaluza software (v2.1, Beckman Coulter).

8. RNA extraction and RT-qPCR

Cells were sorted into RLT lysis buffer (Qiagen) with 1% β-mercaptoethanol. RNA was extracted with RNeasy MicroKit (Qiagen) according to the manufacturer's instructions. RNA was reversely transcribed into cDNA using Superscript IV (Invitrogen). RT-qPCR was performed with absolute qPCR SYBR Green Mix (Thermo Fisher Scientific) using Roche Lightcycler™ 175. mRNA levels were normalized to *Gapdh* as housekeeping gene.

Gene	Forward (5'-3')	Reverse (3'-5')
Gapdh	ACTCCACTCACGGCAAATTC	TCTCCATGGTGGTGAAGACA
Ccr2	ACAGCTCAGGATTAACAGGGACTTG	ACCACTTGCATGCACACATGAC
Cd115	TGTCATCGAGCCTAGTGGC	CGGGAGATTCAGGGTCCAAG
Itgam	ATTTTACCGGACTGCGTGGA	CCCATGGCACTCATGGTGAT
Cd74	GCTGGATGAAGCAGTGGCTCTT	GATGTGGCTGACTTCTTCCTGG
Ms4a3	GTGGTTCTGTTTATCAGCCCTT	ACAGTGGGTAGCCTGTGTAGA

9. Bulk RNA sequencing:

For bulk RNA sequencing, described populations were sorted into Rneasy Microkit (Qiagen) lysis buffer containing 1% β-mercaptoethanol. RNA was extracted following

manufacturer's protocol. To insure appropriate RNA amounts, samples from two mice were pooled for n=1 in both conditions.

Bulk RNA sequencing was performed by CeGat (Tübingen, Germany). Sequencing was performed with 2 x 100 bp read length and 50 million clusters/probe on NovaSeq 6000 (Illumina). Normalization data was provided by CeGat. Group comparison was done using Deseq2 in R. PCA plots were done using Deseq2 in R. GO terms were analysed with the online tool “g:Profiler”[54].

10. Single-cell RNA sequencing:

Dura mater was prepared from five infected and six control *Wt* mice as described above in section 5.

Prior FACS, cells from individual control or infected mice were labelled using the 10X 3' CellPlex Kit Set A (PN-1000261).

For single-cell RNA sequencing the transcript library was established using 10x genomics Chromium Next GEM Single Cell 3' Reagent Kits using the instructions provided by the manufacturer. Single cell samples were processed using the 10X Chromium Next GEM Single Cell 3’ Kit v3.1 (PN-1000269), following the manufacturer’s guidelines. In total, 5-6 individual animals per group were pooled after FACS. For controls, around 10 750 cells were sorted per mouse (64 500 cells in total), and for infected mice, in average 11 600 cells were sorted per mouse (46 400 cells in total). Following droplet generation, barcoded single cell RNA-sequencing dual index libraries for 3’ gene expression and cell multiplexing were generated according to the manufacturer’s specifications. Library quality was assessed using Agilent TapeStation 4150, using Cell-free DNA ScreenTape assay (cat. no. 5067-5630) and NEBNext Library Quant Kit for Illumina (cat. no. E7630S). The single cell libraries were sequenced using Ilumina NextSeq1000/2000, with a minimum targeted sequencing depth of 20,000 reads per cell. Fastq files were aligned using the CellRanger software version 7.1.

11. Single-cell RNA sequencing downstream analysis

Downstream analyses were conducted in the R version 4.2.0 programming environment using the Seurat package version 4. All data sets were filtered to remove cells with more than 5% mitochondrial transcripts, with less than 200 or more than 5000 detectable genes. Data was integrated from two separate experiments using the SCtransform algorithm within Seurat. 2000 features were identified using

SelectIntegrationFeatures() and used in PrepSCTIntegration() and FindIntegrationAnchors(). These anchors were used on IntegrateData(). The top 30 PCAs were used for Umap calculation. FindNeighbors() and FindClusters() were calculated with the top 30 dimensions each. For the latter, a resolution of 0.299 was chosen as the highest resolution where every cluster was distinguishable by specific biological functions. Core markers were identified using the FindAllMarkers functions using a threshold of at least 25% of cells expressing the gene and only returning positive values. All clusters are displayed in the respective Violin plots generated by VlnPlot() and sorted according to the respective median.

12. Immunofluorescence staining:

After transcardial perfusion with ice-cold PBS, brain was removed, post-fixed in 4% PFA for 24 h and cryoprotected in 30% sucrose at 4°C until it sank (1-2 days). After tissue freezing in OCT compound (Sakura, Zoeterwoude, Netherlands) on dry ice, the brain was cut in 30-40 µm sagittal cryosections. Sections were firstly permeabilised for 2h using 0.2% Triton-X in PBS, after which the samples were blocked in blocking solution containing 10% goat serum and 0.1% Triton-X. Samples were stained with mastermix containing 5% goat serum in 0.05% Triton-X and antibodies overnight at 4°C. Dilutions of antibodies were 1:500 for Iba-1 (WACO, Japan), 1:200 for anti-GBS (Invitrogen), 1:100 for Ly6C and CD206 (Biolegend). After washing 5x with PBS, samples are incubated for 2h at RT with secondary antibody (goat anti-rabbit Alexa Fluor633 1:500, anti-GFP DyLight488 1:1000 for enhancing endogenous signal in *Cx3Cr1*$^{/gfp}$ mice) and DAPI (1:1000). Samples were washed 5x and mounted on SuperFrost slides using ProLong Diamond Antifade Mountant (Invitrogen).

Whole mounts of dura mater were prepared as previously described[17], with minor modifications. After transcardial perfusion with ice-cold PBS, calvaria containing cortical dura mater was placed in 4% PFA overnight at 4°C. The dura was dissected and placed into PBS overnight at 4°C to remove any PFA. Samples were then blocked for 2h with agitation on RT using a blocking solution containing 5% goat serum and 0.1% Triton-X. Samples were stained overnight at 4°C in staining solution containing 2% goat serum, 0.1% Triton-X and primary antibodies. Primary antibodies used are as follows: anti-GBS (1:200), CD206 (1:100). Nuclei were stained by DAPI (1:1000).

Washing was done 5x with PBS before using the secondary antibodies diluted in a staining solution. Samples were incubated for 2 h at RT. Stained samples were washed thoroughly with PBS and mounted using ProLong Diamond Antifade Mountant.

13. Confocal microscopy of brain sections and dural whole mounts

Confocal microscopy of sagittal brain slices or dural whole mounts was performed with LSM 880 or LSM 980 confocal microscopes equipped with a 20 × /0.8 NA Plan-Apochromat objective (Carl Zeiss Microimaging) using 1-1.5 µm optical slices. Images are displayed as maximum-intensity projections of 25-40µm thick z stacks, 1024x1024 pixel resolution.

14. Image analysis and processing for 3DMorph

For reconstruction of MG cells, 40 µm sagittal brain slices were imaged with LSM 980 confocal microscope (Carl Zeis Microimaing) using 1 µm optical slices. A MATLAB-based program, 3DMorph, was used to perform unbiased and automatic analysis of microglial morphometric parameters. All images were processed with the following settings: Otsu thresholding 0.5 – 1.0; noise filtration 200 – 500. Largest and smallest cells were defined on a per-image basis to maximize cell yield. Lastly, cells analyzed were quality controlled in 3D. Cells localized on image borders in the X, Y, or Z plane were excluded from analysis.

15. ELISA

For brain ELISA, one brain hemisphere was weighed and stored in 1 ml of homogenization buffer (50 mM Tris pH 8, 150 mM NaCl, 5 mM EDTA) containing 10 µl phosphatase and protease inhibitors (Pierce). Brain was then homogenized using tissue lyser (Quiagen™ TissueLyser) with 50/s oscillations for 5 min with 3 mm tungsten carbide beads. Tissue debris was removed by centrifugation at 20 000 g for 10 min at 4°C. Supernatants were kept at -80°C until the analysis. For plasma ELISA, blood was collected into Microvette® tube (Sarstedt) and centrifuged at 10 000 g for 10 min. Plasma was collected and kept at -80°C until the analysis. Concentrations of IL-6, TNF-α, IL-1β and IFN-β were measured using mouse R&D Duo set ELISA kits according to the manufacturer's instructions (R&D Systems).

16. Statistical analysis

The analysis used for each experiment can be found in figure legends, with the number of replicates and independent experiments. Differences were considered statistically significant if p-values were < 0.05. (ns, not significant; *p < 0.05; **p < 0.01;
380 ***p < 0.001; ****p < 0.0001). Data are represented as mean ± SEM if not stated otherwise. GraphPad prism version 10.0.0 was used for statistical analysis.

6. References

1. Kolter, J. & Henneke, P. Codevelopment of Microbiota and Innate Immunity and the Risk for Group B Streptococcal Disease. *Front. Immunol.* **8**, 1497 (2017).
2. Kohli-Lynch, M. *et al.* Neurodevelopmental Impairment in Children After Group B Streptococcal Disease Worldwide: Systematic Review and Meta-analyses. *Clin. Infect. Dis.* **65**, S190–S199 (2017).
3. Seale, A. C. *et al.* Estimates of the Burden of Group B Streptococcal Disease Worldwide for Pregnant Women, Stillbirths, and Children. *Clin. Infect. Dis.* **65**, S200–S219 (2017).
4. Rua, R. *et al.* Infection drives meningeal engraftment by inflammatory monocytes that impairs CNS immunity. *Nat. Immunol.* **20**, 407–419 (2019).
5. Rebejac, J. *et al.* Meningeal macrophages protect against viral neuroinfection. *Immunity* **55**, 2103-2117.e10 (2022).
6. Gres, V., Kolter, J., Erny, D. & Henneke, P. The role of CNS macrophages in streptococcal meningoencephalitis. *J. Leukoc. Biol.* **106**, 209–218 (2019).
7. Prinz, M., Erny, D. & Hagemeyer, N. Ontogeny and homeostasis of CNS myeloid cells. *Nat. Immunol.* **18**, 385–392 (2017).
8. Alves De Lima, K., Rustenhoven, J. & Kipnis, J. Meningeal Immunity and Its Function in Maintenance of the Central Nervous System in Health and Disease. *Annu. Rev. Immunol.* **38**, 597–620 (2020).
9. Van Hove, H. *et al.* A single-cell atlas of mouse brain macrophages reveals unique transcriptional identities shaped by ontogeny and tissue environment. *Nat. Neurosci.* **22**, 1021–1035 (2019).
10. Rustenhoven, J. *et al.* Functional characterization of the dural sinuses as a neuroimmune interface. *Cell* **184**, 1000-1016.e27 (2021).
11. Mazzitelli, J. A. *et al.* Cerebrospinal fluid regulates skull bone marrow niches via direct access through dural channels. *Nat. Neurosci.* **25**, 555–560 (2022).
12. Cugurra, A. *et al.* Skull and vertebral bone marrow are myeloid cell reservoirs for the meninges and CNS parenchyma. *Science* **373**, eabf7844 (2021).
13. Pulous, F. E. *et al.* Cerebrospinal fluid can exit into the skull bone marrow and instruct cranial hematopoiesis in mice with bacterial meningitis. *Nat. Neurosci.* **25**, 567–576 (2022).
14. Ajami, B., Bennett, J. L., Krieger, C., McNagny, K. M. & Rossi, F. M. V. Infiltrating monocytes trigger EAE progression, but do not contribute to the resident microglia pool. *Nat. Neurosci.* **14**, 1142–1149 (2011).
15. Ritzel, R. M. *et al.* Functional differences between microglia and monocytes after ischemic stroke. *J. Neuroinflammation* **12**, 1–12 (2015).

16. Lehnardt, S. *et al.* A Mechanism for Neurodegeneration Induced by Group B Streptococci through Activation of the TLR2/MyD88 Pathway in Microglia. *J. Immunol.* **177**, 583–592 (2006).
17. Pinho-Ribeiro, F. A. *et al.* Bacteria hijack a meningeal neuroimmune axis to facilitate brain invasion. *Nature* **615**, 472–481 (2023).
18. A, T. *et al.* Group B Streptococcus surface proteins as major determinants for meningeal tropism. *Curr. Opin. Microbiol.* **15**, (2012).
19. B, P. *et al.* Regulation of PI-2b Pilus Expression in Hypervirulent Streptococcus agalactiae ST-17 BM110. *PloS One* **12**, (2017).
20. Ce, H. *et al.* Increased plasma levels of interleukin-6 in sepsis. *Blood* **74**, (1989).
21. Sharief, M. K., Ciardi, M. & Thompson, E. J. Blood-Brain Barrier Damage in Patients with Bacterial Meningitis: Association with Tumor Necrosis Factor- but not Interleukin-I. *J. Infect. Dis.* **166**, 350–358 (1992).
22. Djukic, M. Circulating monocytes engraft in the brain, differentiate into microglia and contribute to the pathology following meningitis in mice. *Brain* **129**, 2394–2403 (2006).
23. Masuda, T. *et al.* Specification of CNS macrophage subsets occurs postnatally in defined niches. *Nature* **604**, 740–748 (2022).
24. Askew, K. *et al.* Coupled Proliferation and Apoptosis Maintain the Rapid Turnover of Microglia in the Adult Brain. *Cell Rep.* **18**, 391–405 (2017).
25. Prinz, M., Jung, S. & Priller, J. Microglia Biology: One Century of Evolving Concepts. *Cell* **179**, 292–311 (2019).
26. Erny, D. *et al.* Host microbiota constantly control maturation and function of microglia in the CNS. *Nat. Neurosci.* **18**, 965–977 (2015).
27. Bosch, L. F. P. & Kierdorf, K. The Shape of µ-How Morphological Analyses Shape the Study of Microglia. *Front. Cell. Neurosci.* **16**, 942462 (2022).
28. York, E. M., LeDue, J. M., Bernier, L.-P. & MacVicar, B. A. 3DMorph Automatic Analysis of Microglial Morphology in Three Dimensions from *Ex Vivo* and *In Vivo* Imaging. *eneuro* **5**, ENEURO.0266-18.2018 (2018).
29. Vidal-Itriago, A. *et al.* Microglia morphophysiological diversity and its implications for the CNS. *Front. Immunol.* **13**, 997786 (2022).
30. Cronk, J. C. *et al.* Peripherally derived macrophages can engraft the brain independent of irradiation and maintain an identity distinct from microglia. *J. Exp. Med.* **215**, 1627–1647 (2018).
31. Bennett, F. C. *et al.* A Combination of Ontogeny and CNS Environment Establishes Microglial Identity. *Neuron* **98**, 1170-1183.e8 (2018).

32. Werner, Y. *et al.* Cxcr4 distinguishes HSC-derived monocytes from microglia and reveals monocyte immune responses to experimental stroke. *Nat. Neurosci.* **23**, 351–362 (2020).
33. Huang, Y. *et al.* Repopulated microglia are solely derived from the proliferation of residual microglia after acute depletion. *Nat. Neurosci.* **21**, 530–540 (2018).
34. Goldmann, T. *et al.* Origin, fate and dynamics of macrophages at central nervous system interfaces. *Nat. Immunol.* **17**, 797–805 (2016).
35. Van Hove, H. *et al.* A single-cell atlas of mouse brain macrophages reveals unique transcriptional identities shaped by ontogeny and tissue environment. *Nat. Neurosci.* **22**, 1021–1035 (2019).
36. Mrdjen, D. *et al.* High-Dimensional Single-Cell Mapping of Central Nervous System Immune Cells Reveals Distinct Myeloid Subsets in Health, Aging, and Disease. *Immunity* **48**, 380-395.e6 (2018).
37. Mildner, A. *et al.* Ly-6G+CCR2− Myeloid Cells Rather Than Ly-6ChighCCR2+ Monocytes Are Required for the Control of Bacterial Infection in the Central Nervous System. *J. Immunol.* **181**, 2713–2722 (2008).
38. Brioschi, S. *et al.* Heterogeneity of meningeal B cells reveals a lymphopoietic niche at the CNS borders. *Science* (2021) doi:10.1126/science.abf9277.
39. Mildner, A. *et al.* Microglia in the adult brain arise from Ly-6ChiCCR2+ monocytes only under defined host conditions. *Nat. Neurosci.* **10**, 1544–1553 (2007).
40. Geissmann, F., Jung, S. & Littman, D. R. Blood Monocytes Consist of Two Principal Subsets with Distinct Migratory Properties. *Immunity* **19**, 71–82 (2003).
41. Yáñez, A. *et al.* Granulocyte-Monocyte Progenitors and Monocyte-Dendritic Cell Progenitors Independently Produce Functionally Distinct Monocytes. *Immunity* **47**, 890-902.e4 (2017).
42. Liu, Z. *et al.* Fate Mapping via Ms4a3-Expression History Traces Monocyte-Derived Cells. *Cell* **178**, 1509-1525.e19 (2019).
43. Trzebanski, S. *et al. Murine GMP- and MDP-Derived Classical Monocytes Have Distinct Functions and Fates*. http://biorxiv.org/lookup/doi/10.1101/2023.07.29.551083 (2023) doi:10.1101/2023.07.29.551083.
44. Lösslein, A. K. *et al.* Monocyte progenitors give rise to multinucleated giant cells. *Nat. Commun.* **12**, 2027 (2021).
45. Hettinger, J. *et al.* Origin of monocytes and macrophages in a committed progenitor. *Nat. Immunol.* **14**, 821–830 (2013).
46. Schain, A. J. *et al.* Activation of pial and dural macrophages and dendritic cells by cortical spreading depression. *Ann. Neurol.* **83**, 508–521 (2018).

47. Herisson, F. *et al.* Direct vascular channels connect skull bone marrow and the brain surface enabling myeloid cell migration. *Nat. Neurosci.* **21**, 1209–1217 (2018).
48. Barth, M. W., Hendrzak, J. A., Melnicoff, M. J. & Morahan, P. S. Review of the macrophage disappearance reaction. *J. Leukoc. Biol.* **57**, 361–367 (1995).
49. Louwe, P. A. *et al.* Recruited macrophages that colonize the post-inflammatory peritoneal niche convert into functionally divergent resident cells. *Nat. Commun.* **12**, 1–15 (2021).
50. Blériot, C. *et al.* Liver-resident macrophage necroptosis orchestrates type 1 microbicidal inflammation and type-2-mediated tissue repair during bacterial infection. *Immunity* **42**, (2015).
51. Sm, L. *et al.* Organ-Specific Fate, Recruitment, and Refilling Dynamics of Tissue-Resident Macrophages during Blood-Stage Malaria. *Cell Rep.* **25**, (2018).
52. Kim, B. J. *et al.* Streptococcus agalactiae disrupts P-glycoprotein function in brain endothelial cells. *Fluids Barriers CNS* **16**, 26 (2019).
53. Doran, K. S. *et al.* Blood-brain barrier invasion by group B *Streptococcus* depends upon proper cell-surface anchoring of lipoteichoic acid. *J. Clin. Invest.* **115**, 2499–2507 (2005).
54. Kolberg, L. *et al.* g:Profiler—interoperable web service for functional enrichment analysis and gene identifier mapping (2023 update). *Nucleic Acids Res.* **51**, W207–W212 (2023).

Figure 1

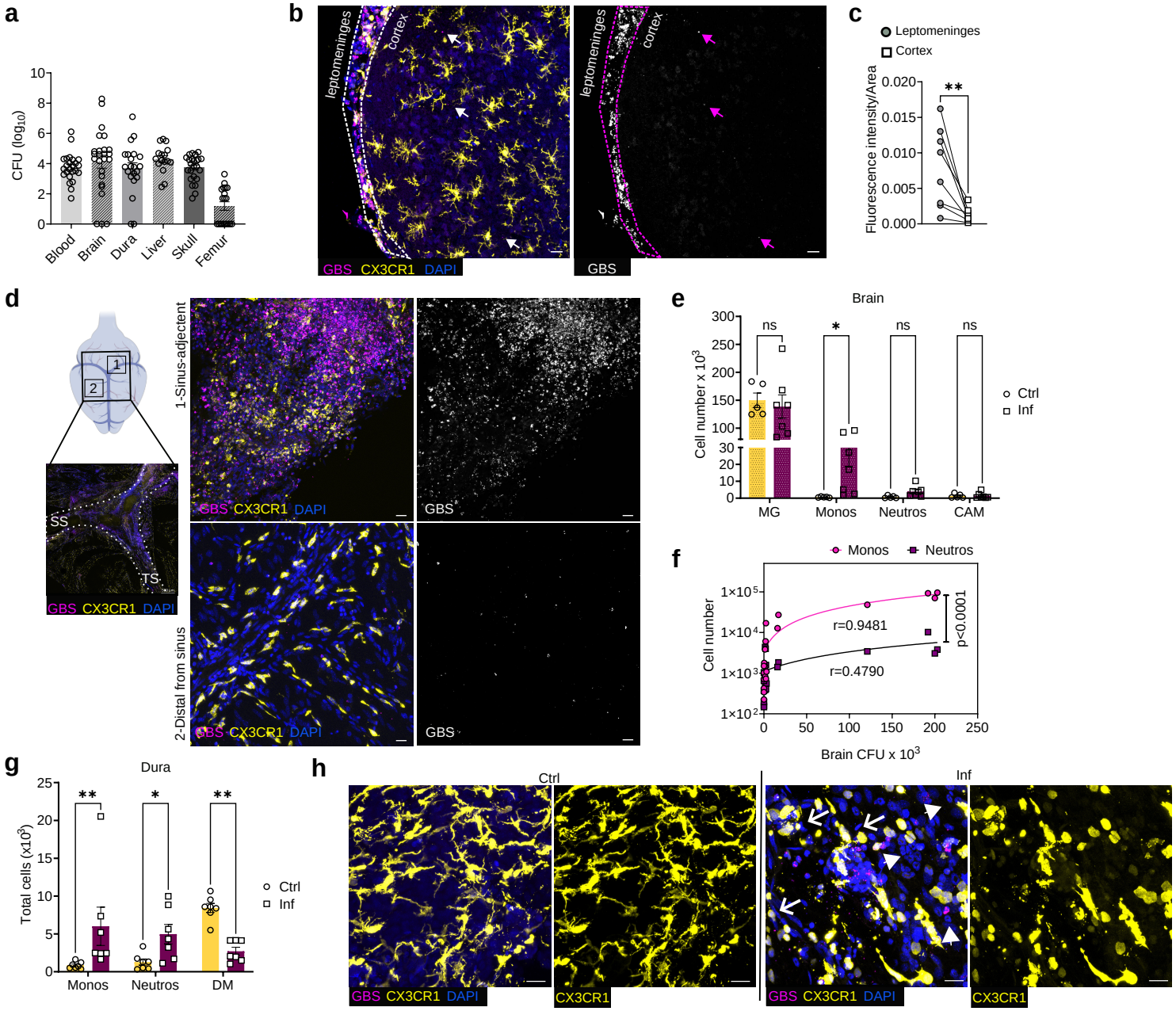
a
CFU (log10)
Blood
Brain
Dura
Liver
Skull
Femur
b
leptomeninges
cortex
GBS CX3CR1 DAPI
GBS
c
Leptomeninges
Cortex
Fluorescence intensity/Area
**
d
1-Sinus-adjectent
2-Distal from sinus
SS
TS
GBS CX3CR1 DAPI
GBS
e
Brain
Cell number x 10^3
ns
*
ns
ns
MG
Monos
Neutros
CAM
Ctrl
Inf
f
Monos
Neutros
Cell number
r=0.9481
r=0.4790
p<0.0001
Brain CFU x 10^3
g
Dura
Total cells (x10^3)
**
*
**
Monos
Neutros
DM
Ctrl
Inf
h
Ctrl
Inf
GBS CX3CR1 DAPI
CX3CR1

Figure 2

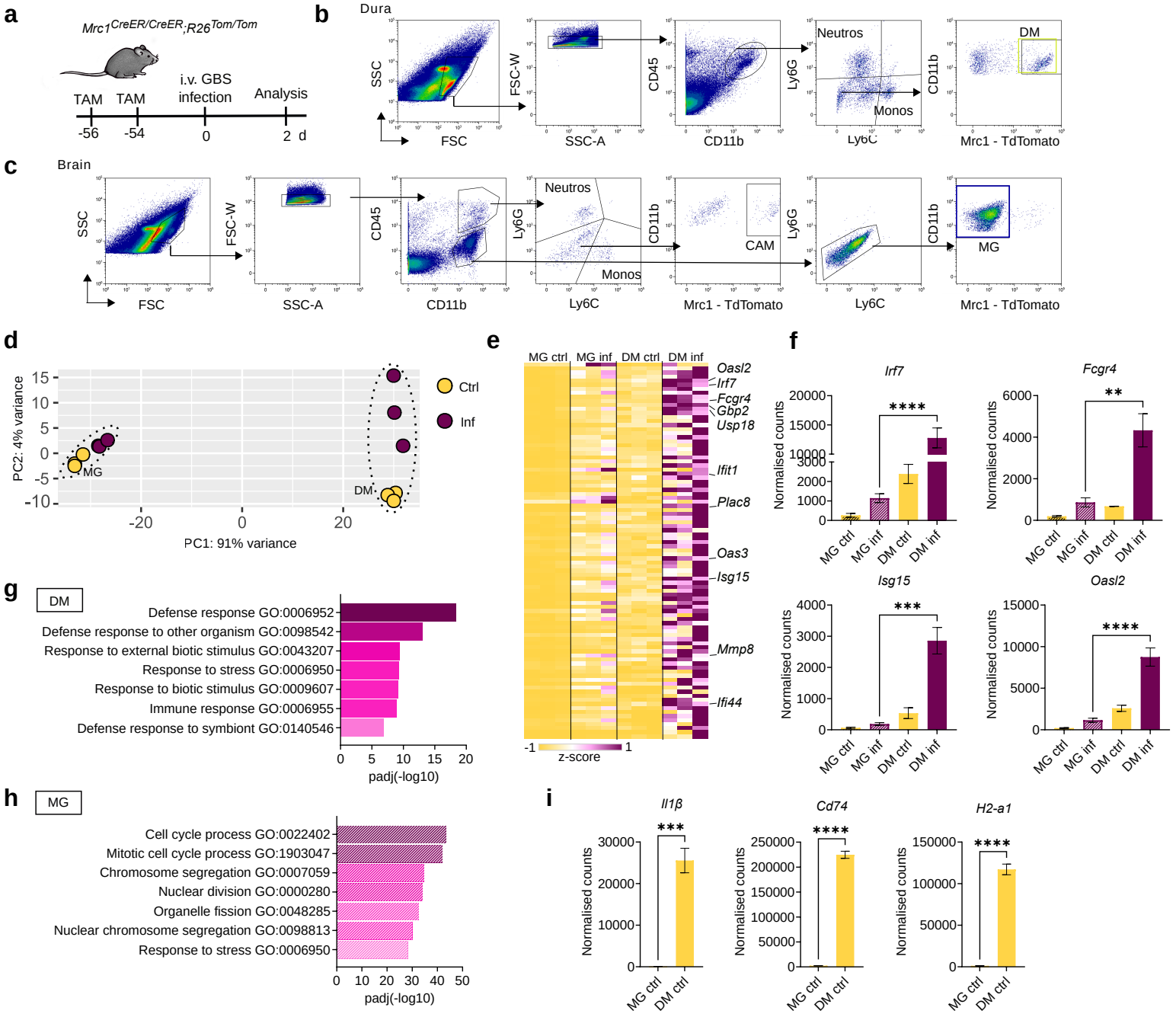
a
Mrc1CreER/CreER;R26Tom/Tom
TAM
TAM
i.v. GBS infection
Analysis
-56
-54
0
2 d
b
Dura
SSC
FSC
FSC-W
SSC-A
CD45
CD11b
Ly6G
Ly6C
Neutros
Monos
DM
Mrc1 - TdTomato
c
Brain
Neutros
Monos
CAM
MG
d
PC2: 4% variance
PC1: 91% variance
Ctrl
Inf
MG
DM
e
MG ctrl
MG inf
DM ctrl
DM inf
Oasl2
Irf7
Fcgr4
Gbp2
Usp18
Ifit1
Plac8
Oas3
Isg15
Mmp8
Ifi44
z-score
f
Irf7
Fcgr4
Isg15
Oasl2
Normalised counts
MG ctrl
MG inf
DM ctrl
DM inf
g
DM
Defense response GO:0006952
Defense response to other organism GO:0098542
Response to external biotic stimulus GO:0043207
Response to stress GO:0006950
Response to biotic stimulus GO:0009607
Immune response GO:0006955
Defense response to symbiont GO:0140546
padj(-log10)
h
MG
Cell cycle process GO:0022402
Mitotic cell cycle process GO:1903047
Chromosome segregation GO:0007059
Nuclear division GO:0000280
Organelle fission GO:0048285
Nuclear chromosome segregation GO:0098813
Response to stress GO:0006950
padj(-log10)
i
Il1β
Cd74
H2-a1
Normalised counts
MG ctrl
DM ctrl

Figure 3

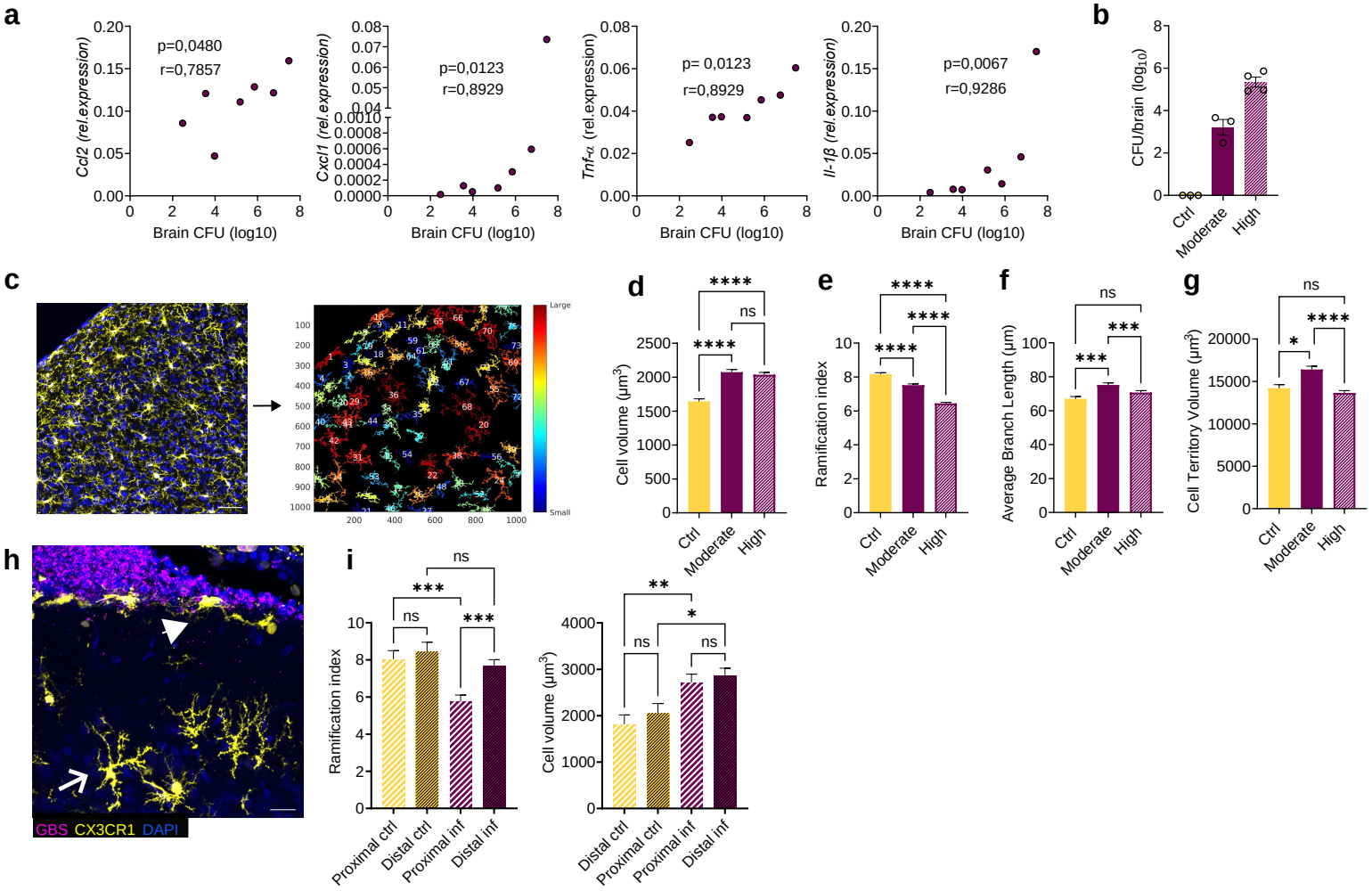
a
p=0,0480
r=0,7857
Ccl2 (rel.expression)
p=0,0123
r=0,8929
Cxcl1 (rel.expression)
p= 0,0123
r=0,8929
Tnfα (rel.expression)
p=0,0067
r=0,9286
Il-1β (rel.expression)
Brain CFU (log10)
b
CFU/brain (log10)
Ctrl
Moderate
High
c
Large
Small
d
Cell volume (µm³)
e
Ramification index
f
Average Branch Length (µm)
g
Cell Territory Volume (µm³)
h
GBS CX3CR1 DAPI
i
Ramification index
Cell volume (µm³)
Proximal ctrl
Distal ctrl
Proximal inf
Distal inf
ns

Figure 4

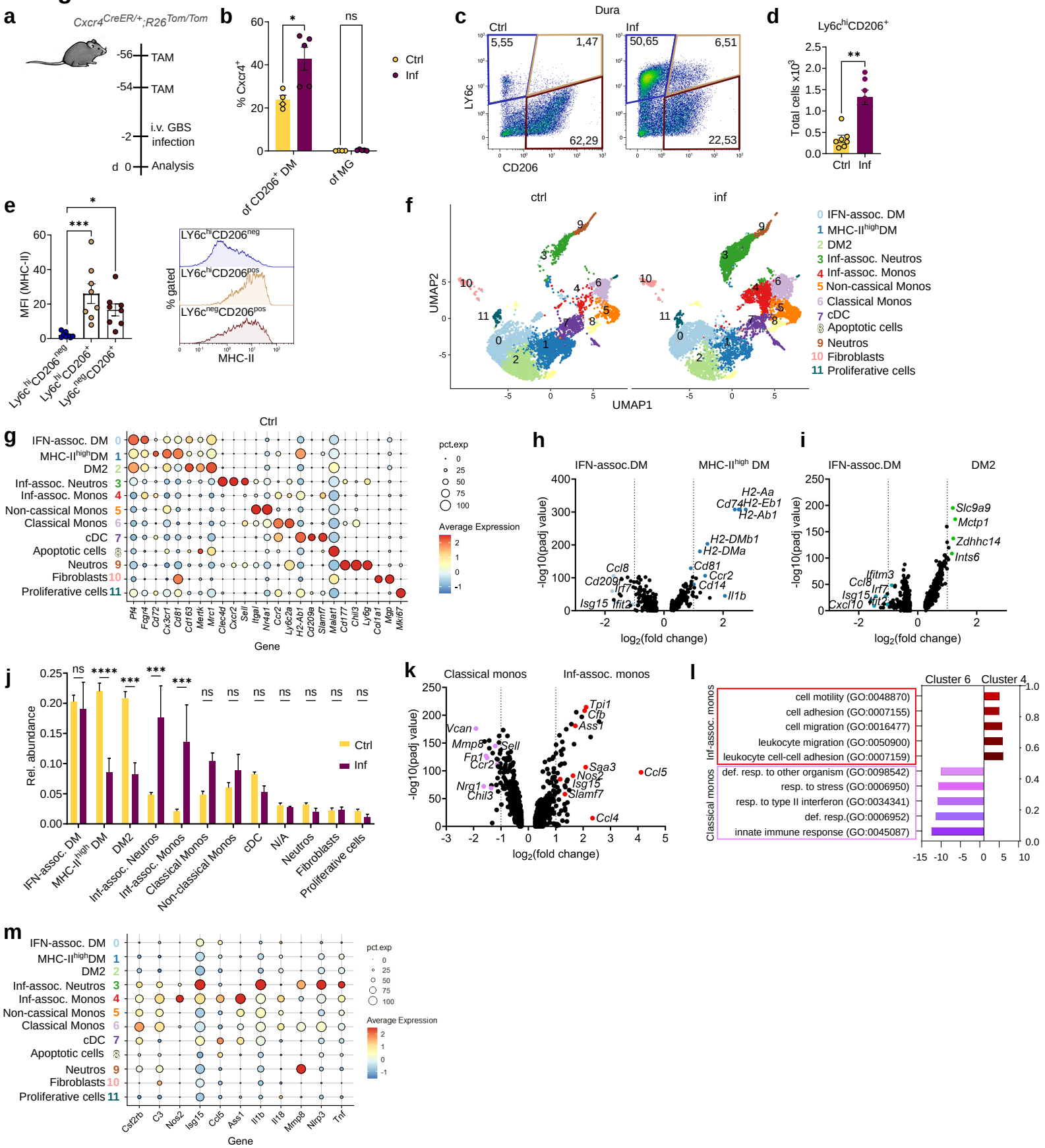
a
Cxcr4CreER/+;R26Tom/Tom
-56 TAM
-54 TAM
-2 i.v. GBS infection
d 0 Analysis
b
% Cxcr4+
of CD206+ DM
of MG
Ctrl
Inf
c
Dura
Ctrl
Inf
LY6c
CD206
d
Ly6chiCD206+
Total cells x10^3
Ctrl
Inf
e
MFI (MHC-II)
Ly6chiCD206neg
Ly6chiCD206+
Ly6cnegCD206+
% gated
MHC-II
f
ctrl
inf
UMAP2
UMAP1
0 IFN-assoc. DM
1 MHC-IIhighDM
2 DM2
3 Inf-assoc. Neutros
4 Inf-assoc. Monos
5 Non-cassical Monos
6 Classical Monos
7 cDC
8 Apoptotic cells
9 Neutros
10 Fibroblasts
11 Proliferative cells
g
Ctrl
Gene
pct.exp
Average Expression
h
IFN-assoc.DM
MHC-IIhigh DM
-log10(padj value)
log2(fold change)
i
IFN-assoc.DM
DM2
-log10(padj value)
log2(fold change)
j
Rel. abundance
Ctrl
Inf
IFN-assoc. DM
MHC-IIhigh DM
DM2
Inf-assoc. Neutros
Inf-assoc. Monos
Classical Monos
Non-classical Monos
cDC
N/A
Neutros
Fibroblasts
Proliferative cells
k
Classical monos
Inf-assoc. monos
-log10(padj value)
log2(fold change)
l
Cluster 6
Cluster 4
Inf-assoc. monos
cell motility (GO:0048870)
cell adhesion (GO:0007155)
cell migration (GO:0016477)
leukocyte migration (GO:0050900)
leukocyte cell-cell adhesion (GO:0007159)
Classical monos
def. resp. to other organism (GO:0098542)
resp. to stress (GO:0006950)
resp. to type II interferon (GO:0034341)
def. resp.(GO:0006952)
innate immune response (GO:0045087)
m
Gene
pct.exp
Average Expression

Figure 5

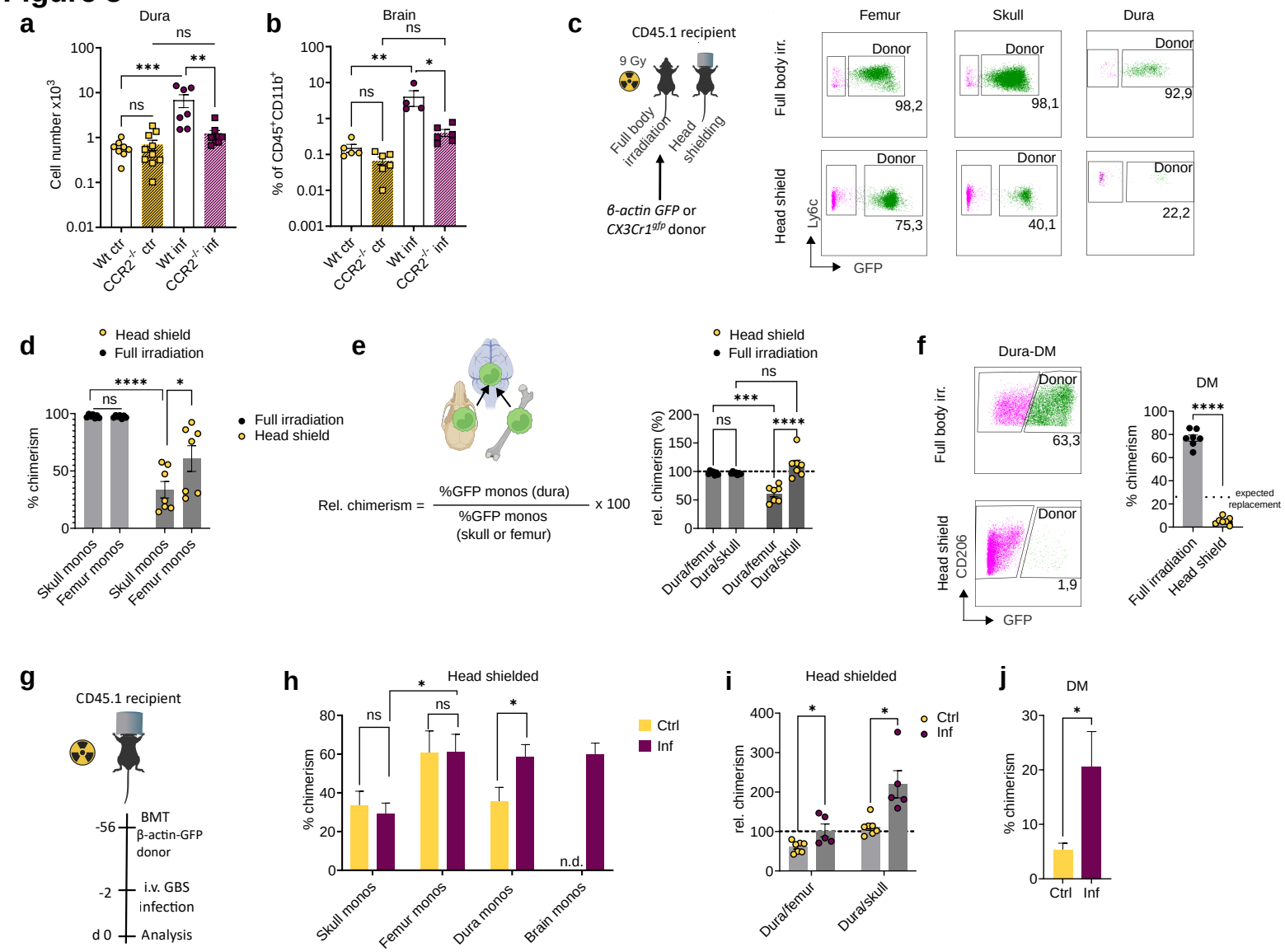
a
Dura
Cell number x10^3
Wt ctr
CCR2-/- ctr
Wt inf
CCR2-/- inf
b
Brain
% of CD45+CD11b+
c
CD45.1 recipient
9 Gy
Full body irradiation
Head shielding
β-actin GFP or CX3Cr1gfp donor
Femur
Skull
Dura
Full body irr.
Head shield
Donor
98,2
98,1
92,9
75,3
40,1
22,2
Ly6c
GFP
d
Head shield
Full irradiation
% chimerism
Skull monos
Femur monos
e
Rel. chimerism = %GFP monos (dura) / %GFP monos (skull or femur) x 100
rel. chimerism (%)
Dura/femur
Dura/skull
f
Dura-DM
63,3
1,9
CD206
DM
expected replacement
Full irradiation
Head shield
g
CD45.1 recipient
BMT
β-actin-GFP donor
i.v. GBS infection
Analysis
h
Head shielded
Ctrl
Inf
n.d.
Skull monos
Femur monos
Dura monos
Brain monos
i
Head shielded
rel. chimerism
j
DM
Ctrl
Inf

Figure 6

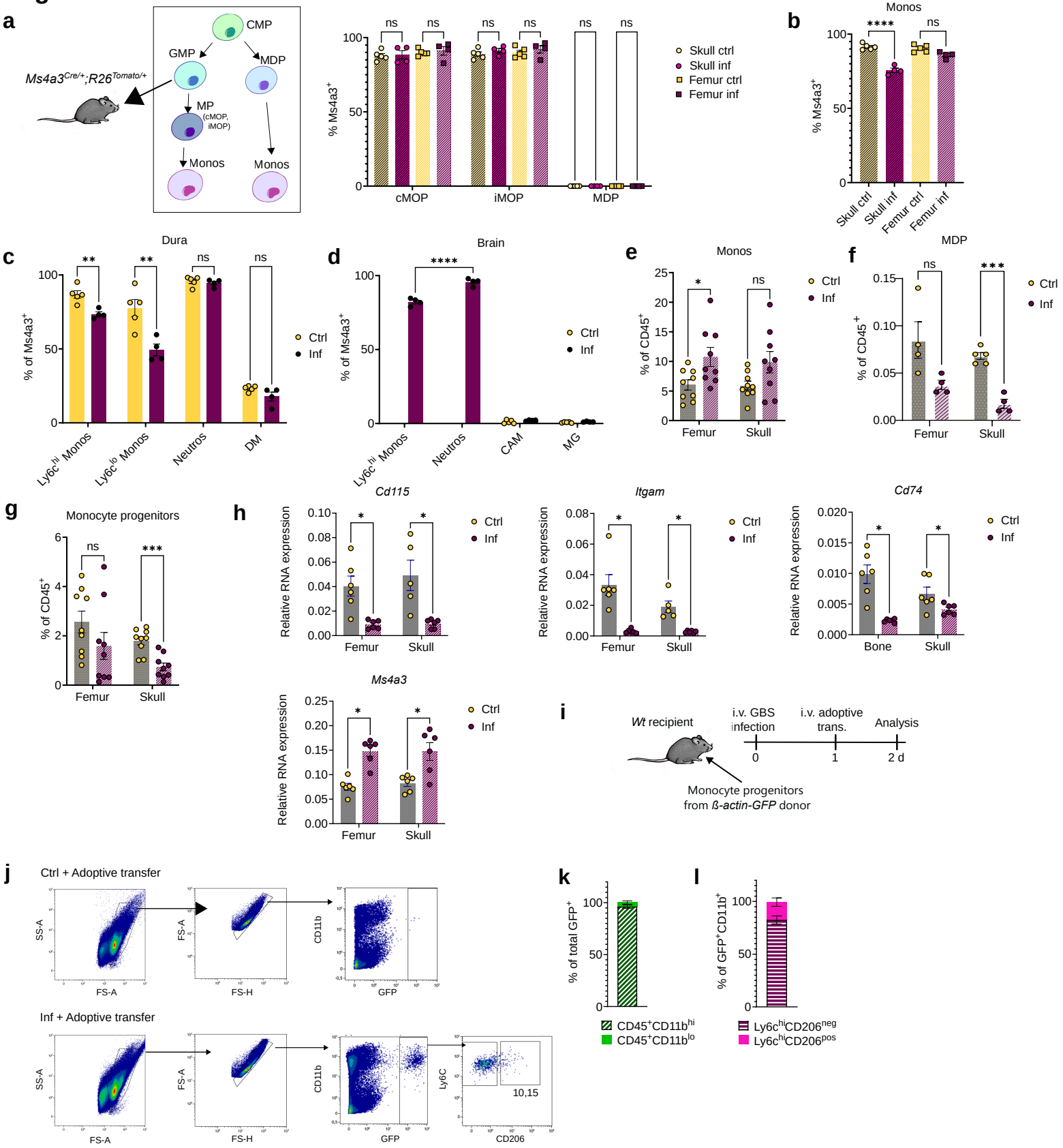
a
Ms4a3Cre/+;R26Tomato/+
CMP
GMP
MDP
MP
(cMOP, iMOP)
Monos
Monos
% Ms4a3+
cMOP
iMOP
MDP
Skull ctrl
Skull inf
Femur ctrl
Femur inf
b
Monos
% Ms4a3+
Skull ctrl
Skull inf
Femur ctrl
Femur inf
c
Dura
% of Ms4a3+
Ly6c hi Monos
Ly6c lo Monos
Neutros
DM
Ctrl
Inf
d
Brain
% of Ms4a3+
Ly6c hi Monos
Neutros
CAM
MG
Ctrl
Inf
e
Monos
% of CD45+
Femur
Skull
Ctrl
Inf
f
MDP
% of CD45+
Femur
Skull
Ctrl
Inf
g
Monocyte progenitors
% of CD45+
Femur
Skull
h
Cd115
Relative RNA expression
Femur
Skull
Ctrl
Inf
Itgam
Relative RNA expression
Femur
Skull
Ctrl
Inf
Cd74
Relative RNA expression
Bone
Skull
Ctrl
Inf
Ms4a3
Relative RNA expression
Femur
Skull
Ctrl
Inf
i
Wt recipient
i.v. GBS infection
i.v. adoptive trans.
Analysis
0
1
2 d
Monocyte progenitors from ß-actin-GFP donor
j
Ctrl + Adoptive transfer
SS-A
FS-A
FS-A
FS-H
CD11b
GFP
Inf + Adoptive transfer
SS-A
FS-A
FS-A
FS-H
CD11b
GFP
Ly6C
CD206
10,15
k
% of total GFP+
CD45+CD11bhi
CD45+CD11blo
l
% of GFP+CD11b+
Ly6chiCD206neg
Ly6chiCD206pos